J. Fluid Mech. (2013), *vol.* 729, *pp.* 151–179.
doi:10.1017/jfm.2013.292

Large eddy simulation of flow around a reverse rotating propeller

Hyunchul Jang and Krishnan Mahesh†

Aerospace Engineering & Mechanics, University of Minnesota, Minneapolis, MN 55455, USA

(Received 30 January 2012; revised 18 February 2013; accepted 4 June 2013;
first published online 18 July 2013)

This paper studies the flow around a propeller rotating in the reverse direction in a uniform free stream. Large eddy simulation is used to study this massively separated flow at a Reynolds number of 480 000 and advance ratios $J = -0.5$, -0.7 and -1.0. Simulations are performed on two grids; statistics of the loads and velocity field around the propeller show encouraging agreement between the two grids and with experiment. The impact of advance ratio is discussed, and a physical picture of the unsteady flow and its influence on the propeller loads is proposed. An unsteady vortex ring is formed in the vicinity of the propeller disk due to the interaction between the free stream and the reverse flow produced by the reverse rotation. The flow is separated in the blade passages; the most prominent is the separation along the sharp edge of the blade on the downstream side of the blade. This separation results in high-amplitude, transient propeller loads. Conditional averaging is used to describe the statistically relevant events that determine low- and high-amplitude thrust and side-forces. The vortex ring is closer and the reverse flow induced by propeller rotation is lower when the loads are high. The propeller loads scale with ρU^2 for $J < -0.7$ and with $\rho n^2 D^2$ for $J > -0.7$.

Key words: turbulence simulation, turbulent flows

1. Introduction

The flow around propellers has been studied extensively for its applications to noise (Tam & Salikuddin 1986; Amiet 1988; Chapman 1988; Parry 1995; Cooper & Peake 2005), cavitation (Kinnas & Fine 1993; Duttweiler & Brennen 2002), the effects of partial submersion (Furuya 1985), and the nature of propeller wakes (Felli *et al.* 2006). All these studies consider propellers in their 'forward' mode of operation, where the propeller rotates in the direction that produces net thrust. Another fundamental operating condition is termed 'crashback': here the vehicle decelerates because the propeller rotates in the reverse direction while the direction of the free stream remains the same. Denoting the free-stream and propeller angular velocities by U and ω respectively, the forward and crashback modes correspond to $(U > 0, \omega > 0)$ and $(U > 0, \omega < 0)$, respectively.

As might be anticipated, the flow around propellers in crashback has a strongly negative angle of attack and naturally triggers a massive flow separation at the leading edge; as a result, thrust and torque are highly unsteady and their transient levels

† Email address for correspondence: mahesh@aem.umn.edu

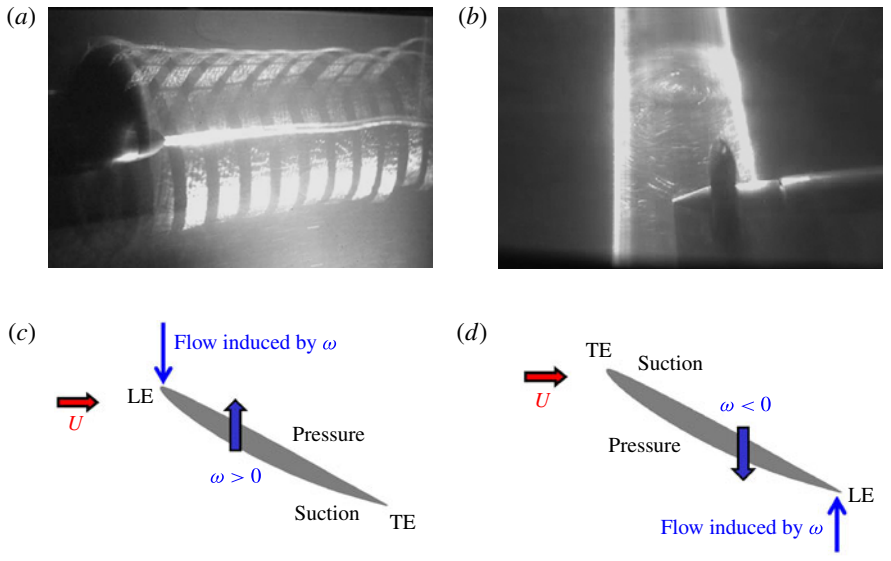

FIGURE 1. (Colour online) (*a*) Flow visualization of forward condition (reprinted with permission from Felli *et al.*, *Exp. Fluids*, vol. 41, 2006). (*b*) Flow visualization of crashback condition (reprinted with permission from Bridges *et al.*, *AIAA paper 2005-236*, 2005). (*c*) Schematic of flow in the blade passage in forward condition. (*d*) Schematic of flow in the blade passage in crashback condition.

can cause blade damage. Also, flow separation induces high levels of unsteady side-forces which impede vehicle manoeuvrability. This paper therefore studies propeller crashback. Figure 1 illustrates the qualitative nature of the flow in crashback, and contrasts it to the flow in the forward mode. When the propeller rotates in the 'forward' direction (figure 1*a*), helical tip vortices are observed along with a hub vortex in the slipstream. In contrast, the flow around the propeller in crashback is dominated by a vortex ring in the vicinity of the propeller disk (figure 1*b*). The flow through the propeller blade passage is fundamentally different; as shown in figure 1(*c,d*), the pressure and suction sides are reversed when the propeller rotates in the reverse direction. The flow through the propeller disk in crashback is therefore opposite to the direction of the free stream, and the leading and trailing edges of the blade exchange their roles when defined with respect to the local flow. Accurate prediction of the crashback flow therefore requires accurate representation of the separated flow inside the blade passages and the unsteady vortex ring outside the propeller disk; it does not require us to capture attached boundary layers. This paper therefore uses the large eddy simulation methodology to simulate propeller crashback.

The crashback flow is similar in some respects to 'rotating stall' in turbomachinery (Staubli, Gyarmathy & Inderbitzen 2001) (figure 2*a*) and the 'vortex ring state' (VRS) observed during helicopter hover (figure 2*b*). Rotating stall is a well-known instability in compressors, which typically occurs when non-uniform inflow results in a locally high angle of attack, inducing flow separation in a blade passage (figure 2*c*). The resulting blockage diverts the inflow to another blade passage, which then stalls; the stall cell thus propagates in a direction opposite to rotor rotation (Pampreen 1993; Niazi 2000). Although the blade passage flow is stalled in both rotating stall

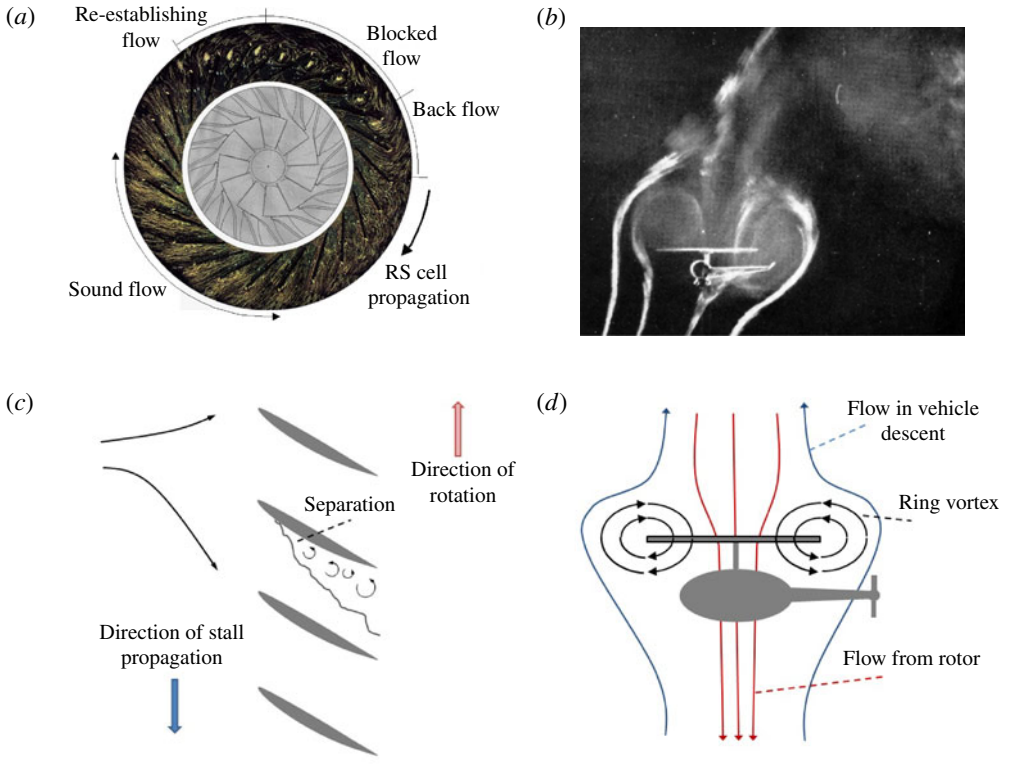

FIGURE 2. (Colour online) (*a*) Flow visualization of rotating stall for turbomachinery (reprinted with permission from Staubli *et al.*, *La Houille Blanche*, vol. 3/4, 2001). (*b*) Flow visualization of the vortex ring state (VRS) for helicopter (reprinted with permission from Drees and Hendal, *Aircraft Engineering and Aerospace Technology*, vol. 23, 1951). (*c*) Schematic of rotating stall. (*d*) Schematic of VRS.

and crashback, note that the rotor continues rotating in the forward direction during rotating stall, unlike in crashback. As a result, the pressure and suction sides remain unchanged, and no vortex ring is observed external to the compressor. Helicopters in vertical descent experience the VRS state, whose onset is usually accompanied by the loss of altitude and controllability (Drees & Hendal 1951; Green, Gillies & Brown 2005; Leishman 2006). Here, the rotor of the helicopter pushes fluid down, while the free stream is in the upward direction with respect to the helicopter as shown in figure 2(*d*). A large unsteady vortex ring forms above the rotor disk as it does in crashback (figure 2*b*).

A brief description of experimental work on crashback follows. The relative strengths of free-stream velocity and propeller rotation are represented by the advance ratio

$$J = \frac{U}{nD}, \tag{1.1}$$

where U is the free-stream velocity, D is the diameter of the propeller disk, and $n = \omega/2\pi$ is the rotational speed of the propeller. Four quadrant evaluations for a series of propellers were conducted by Hecker & Remmers (1971) using open

water (OW) experiments. Thrust and torque coefficients were measured over a wide range of advance ratios. The highly unsteady motion of the vortex ring was observed and visualized by Hampton (1995) with OW and water tunnel (WT) experiments. They noted that the vortex ring oscillated both vertically and horizontally. Jiang *et al.* (1997) measured the propeller-induced flow field at the blade tip region using particle displacement velocimetry (PDV) for propeller P4381. They observed a periodic cycle where the vortex moved downstream, broke into two vortices, and moved back toward the tip. The period of this cycle was equal to the frequency of the side-force oscillations. More recent measurements of flow around the same propeller by Jessup *et al.* (2004) using particle image velocimetry (PIV) and laser Doppler velocimetry (LDV) confirmed the large unsteady vortex ring movement. However, their experiments did not show any obvious cyclic behaviour of the vortex ring. The discrepancy between these experiments was attributed to differences in test section size of water tunnels. Jessup, Fry & Donnelly (2006) and Donnelly, Jessup & Etebari (2008) performed crashback experiments on a ducted propeller. The addition of a duct tended to move the vortex ring outboard and exacerbated the side-force. The experiment by Bridges, Donnelly & Park (2005, 2008) reported the effect of an upstream hull on the marine propeller.

Chen & Stern (1999) conducted unsteady Reynolds-averaged Navier–Stokes (U-RANS) simulation for propeller P4381 over all four quadrants. They showed that RANS yielded good results for forward and backing conditions, but produced significant discrepancies in crashback and crash-ahead conditions. Vyšohlid & Mahesh (2006) performed LES of flow around P4381 at an advance ratio of $J = -0.7$ under the same conditions as experiments by Jessup *et al.* (2004). They showed that the LES yielded good agreement for mean and root mean square (r.m.s.) of unsteady loads as well as spectra. Chang *et al.* (2008) performed LES at other advance ratios, $J = -0.5$ and $J = -1.0$ with the same solver and computational grid as used in Vyšohlid & Mahesh (2006). They investigated instantaneous flow fields at low- and high-amplitude events. Chang *et al.* (2008) also used LES to predict shear and bending stresses on the blade surface, and good agreement was observed. LES was performed for a simple actuator disk model of crashback by Vyšohlid & Mahesh (2007). Verma, Jang & Mahesh (2012) investigated the effect of an upstream submarine hull on a propeller in crashback using the same computational methodology.

The unsteady vortex ring in crashback has been reported, but how the vortex ring is related to unsteady loads has not been studied. Similarly, the physics of the flow that determines extreme load events and the related separated flow in the blade passages have not been statistically characterized. This paper proposes a physical mechanism for the global flow structure (vortex ring), and its relation to the local flow structure (separation vortices on propeller blades). The relation between the flow and the the unsteady loads is also described. The objectives of the paper are to: (i) demonstrate the ability of LES to predict crashback with fidelity; (ii) study the origin of unsteady loads; (iii) use conditional averaging to study the nature of low- and high-amplitude load events; (iv) study the effect of advance ratio; and (v) propose a simple description of the relation between the vortex ring and the flow in the blade passage. The paper is organized as follows. In § 2 we introduce the governing equations, numerical method, and problem description for the crashback simulations. LES is validated against experiments performed by Jessup *et al.* (2004, 2006) at an advance ratio, $J = -0.7$ in § 3.1. The flow physics of crashback is analysed in § 3.2. The origin of unsteady loads is studied in § 3.3, and the nature of extreme-amplitude load events is investigated in § 3.4. The effect of advance ratio is investigated at two

other advance ratios ($J = -0.5$ and $J = -1.0$) in § 3.5. In § 4 we summarize the essential physics of the flow in crashback.

2. Simulation details

2.1. *Governing equations and numerical method*

The simulations are performed in a non-inertial frame of reference that rotates with the propeller. The incompressible Navier–Stokes equations in the rotating frame of reference can be written in terms of either the absolute velocity or the relative velocity. Here, absolute velocity refers to the velocity vector with respect to a fixed frame of reference and relative velocity is defined in the rotating frame of reference. Boundary conditions can be easily specified for the absolute velocity even in the rotating frame of reference. Also, the governing equations in the rotating frame may be formulated in a strongly conservative form (Beddhu, Taylor & Whitfield 1996) or in a form where system rotation produces a source term (Majety 2003). Here, the formulation is chosen to be in the rotating frame of reference with absolute velocity vector as shown:

$$\frac{\partial u_i}{\partial t} + \frac{\partial}{\partial x_j}(u_i u_j - u_i \epsilon_{jkl}\omega_k x_l) = -\frac{\partial p}{\partial x_i} - \epsilon_{ijk}\omega_j u_k + \nu \frac{\partial^2 u_i}{\partial x_j \partial x_j}, \tag{2.1}$$

$$\frac{\partial u_i}{\partial x_i} = 0, \tag{2.2}$$

where u_i is the absolute velocity in the fixed frame, p is the pressure, x_i are coordinates in the rotating frame, ω_j is the angular velocity of the rotating frame, ν is the kinematic viscosity, and ϵ_{ijk} denotes the permutation symbol. The positive ω corresponds to the forward mode of operation for a right-handed propeller. The rotating reference frame rotates with the propeller such that the sign is the same as the propeller rotation, which is negative in crashback.

In LES, large scales are directly computed from the spatially filtered Navier–Stokes equations, while small scales are represented by modelling the subgrid stress. Spatial filtering of (2.1) yields the filtered Navier–Stokes equations in the rotating frame of reference as follows:

$$\frac{\partial \bar{u}_i}{\partial t} + \frac{\partial}{\partial x_j}(\bar{u}_i \bar{u}_j - \bar{u}_i \epsilon_{jkl}\omega_k x_l) = -\frac{\partial \bar{p}}{\partial x_i} - \epsilon_{ijk}\omega_j \bar{u}_k + \nu \frac{\partial^2 \bar{u}_i}{\partial x_j \partial x_j} - \frac{\partial \tau_{ij}}{\partial x_j}, \tag{2.3}$$

$$\frac{\partial \bar{u}_i}{\partial x_i} = 0, \tag{2.4}$$

where the overbar denotes the spatial filter and $\tau_{ij} = \overline{u_i u_j} - \bar{u}_i \bar{u}_j$ is the subgrid stress. The dynamic Smagorinsky model proposed by Germano *et al.* (1991) and modified by Lilly (1992) is used to model the subgrid stress over the simulations.

Equation (2.3) is solved using a numerical method developed by Mahesh, Constantinescu & Moin (2004) for incompressible flows on unstructured grids. The method uses a finite-volume approach and computes the convection and pressure terms to be discretely consistent with kinetic energy conservation in the inviscid limit. This analytical property of the inviscid Navier–Stokes equations ensures robustness without numerical dissipation at high Reynolds numbers. Also, the solution exhibits proper Reynolds number sensitivity. Numerical dissipation can dissipate the small scales and overwhelm the effect of the subgrid-scale model.

The algorithm stores the Cartesian velocities and the pressure at the centroids of the cells, and the face-normal velocities are stored independently at the centroids of the

faces. A predictor–corrector approach is used. The predicted velocities at the control volume centroids are first obtained and then interpolated to obtain the face-normal velocities. The predicted face-normal velocity is projected so that the continuity equation is discretely satisfied. This yields a Poisson equation for pressure which is solved iteratively using an algebraic multigrid method. The pressure field is used to update the Cartesian velocities using a least-squares approach for minimizing the conservation error. Implicit time advancement is performed using the Crank–Nicolson scheme. The algorithm has been validated for a variety of problems over a range of Reynolds numbers (Mahesh *et al.* 2004).

2.2. *Problem description*

Simulations are performed for marine propeller P4381, which is five-bladed, right-handed with variable pitch, has no skew and no rake. The propeller has been used in various experiments (Jiang *et al.* 1997; Jessup *et al.* 2004, 2006; Bridges *et al.* 2008) and computations (Davoudzadeh *et al.* 1997; Chen & Stern 1999; Vyšohlid & Mahesh 2006; Chang *et al.* 2008; Berchiche 2008; Verma *et al.* 2012). Details of the blade and hub geometry are given in Jessup *et al.* (2004).

The present simulation is validated with water tunnel (WT) experiments (Jessup *et al.* 2004, 2006) performed in a 36 inch WT at the Naval Surface Warfare Center, Carderock Division (NSWCCD). The geometry of the WT is shown in figure 3(*a*). Only the test section of the WT is enlarged, while the diameter of the tunnel is only three times larger than the propeller diameter. Since the size of the vortex ring created in crashback might be large enough to interact with the wall of the tunnel, especially at the sharp corner of the test section, a tunnel confinement effect could occur in the WT experiment. Jessup *et al.* (2006) also noted that there was potentially a tunnel effect due to the close proximity of the ring vortex structure to the tunnel nozzle shear layer. Another experimental result (open water: OW) is used for validation; this experiment was conducted at NSWCCD and reported in Ebert, Chang & Mulvihill (2007).

The computational domain is a cylinder with a diameter of $7.0D$ and a length of $14.0D$, where D is the diameter of the propeller disk. Free-stream velocity boundary conditions are specified at the inlet and the far-field boundaries. Convective boundary conditions are prescribed at the exit. Since velocities in the governing equations are specified in the fixed frame of reference, boundary conditions on solid walls are also prescribed in the fixed frame. Thus, boundary conditions on the blades and hub are specified as $\boldsymbol{U} = \boldsymbol{r} \times \boldsymbol{\omega}$, while those on the shaft are prescribed as no-slip boundary conditions. A schematic of the computational domain and boundary conditions is shown in figure 3(*b*).

The computational grid is shown in figure 4. The entire grid is composed of two components (figure 4*a*): a cylindrical subdomain including blades and hub surface, and the outer region of the subdomain. The cylindrical subdomain termed the ‘pillbox’ is filled with tetrahedral elements to match the complex geometry of the propeller, and the outer region consists of hexahedral elements. The diameter of the ‘pillbox’ is $1.17D$ and its length is $0.73D$. Two computational grids are used for the simulation; the fine grid has 19.3 million control volumes, and the coarse grid has 7.7 million control volumes. Table 1 lists information on the computational grids. All surfaces of the propeller are meshed by quadrilateral elements as shown in figure 4(*b*). Four hexahedral element layers are extruded from the blade surface in order to improve resolution near the wall, with the first layer at a height of $0.0017D$. Recall that propeller crashback is inherently a massively separated flow regime. Accurate

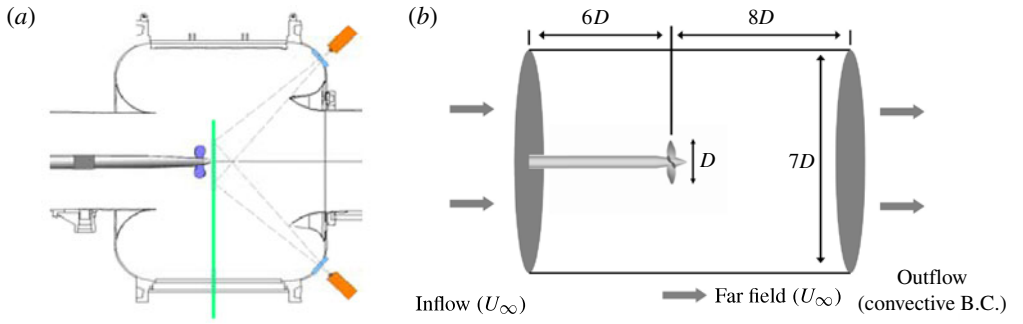

FIGURE 3. (Colour online) (*a*) Geometry of the water tunnel (reprinted with permission from Jessup *et al.*, *26th Symposium on Naval Hydrodynamics*, 2006). (*b*) Computational domain and boundary conditions on domain boundaries.

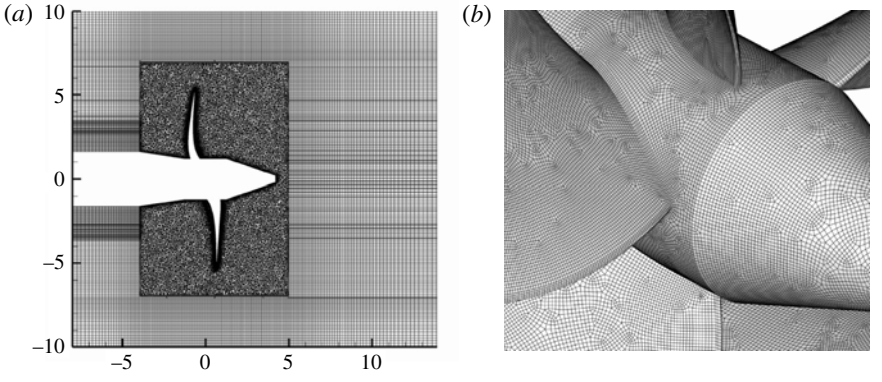

FIGURE 4. Computational grid: (*a*) *x*–*y* plane of the grid, (*b*) surface meshes on the propeller.

Grid	No. of cells in whole domain (millions)	No. of cells in 'pillbox' (millions)	First height	Growth rate
Fine grid	19.3	6.1 (31.8 %)	0.0017*D*	1.05
Coarse grid	7.7	3.3 (42.9 %)	0.0017*D*	1.2

TABLE 1. Information on the computational grids.

prediction of the flow therefore relies not on resolving attached boundary layers but on resolving large-scale coherent motions such as the vortex ring. No wall model is therefore used. A grid sensitivity study will be performed in § 3.1.

3. Results

Simulations are performed under the crashback condition at advance ratios of -0.5, -0.7, and -1.0 at Reynolds number $Re = 480\,000$. The Reynolds number Re is

defined as

$$Re = \frac{DU}{\nu}, \tag{3.1}$$

where U is the free-stream velocity, D is the diameter of the propeller disk, and ν is the kinematic viscosity. According to the experiments of Jessup *et al.* (2004), thrust does not vary with Reynolds number for $4 \times 10^5 < Re < 9 \times 10^5$. The Reynolds number $Re = 480\,000$ is within this range. Detailed comparisons are shown for $J = -0.7$ with time-averaged LDV data of Jessup *et al.* (2004). The computational time step used at for $J = -0.7$ is 0.003, which corresponds to 3.57×10^{-4} rev^{-1}. Additional simulations at $J = -0.5$ and $J = -1.0$ are performed to study the effect of advance ratio in crashback. The corresponding computational time steps at the other advance ratios are 6.67×10^{-3} and 4.17×10^{-3} rev^{-1} at $J = -0.5$ and $J = -1.0$, respectively.

3.1. *Validation of LES at* $J = -0.7$

Results from a grid sensitivity study and a comparison to experimental data are presented. The LES results for mean values, standard deviations and spectra of the loads are compared between coarse and fine grids, and to experiment. The three components of mean velocity and resolved TKE are similarly compared. The effect of the subgrid model is illustrated using the magnitude of the eddy viscosity.

3.1.1. *Magnitude and spectra of unsteady loads*

The highly unsteady flow field produces highly fluctuating loads on the propeller. The thrust T is defined as the axial component of the force exerted on the propeller, and torque Q is the axial component of moment of the force. F_H and F_V denote horizontal and vertical components of the force whose vector sum yields the projected force onto the direction perpendicular to the propeller axis, side-force S. Since computations are performed in a rotating frame of reference, the side-force is transformed to the fixed frame of reference before comparison. Horizontal and vertical components of the side-force, F_H and F_V, are readily obtained by a rotational transformation using the angle between the rotating and the fixed frames. Non-dimensional thrust coefficient K_T, torque coefficient K_Q, and side-force coefficient K_S are defined as

$$K_T = \frac{T}{\rho n^2 D^4}, \quad K_Q = \frac{Q}{\rho n^2 D^5}, \quad K_S = \frac{\sqrt{{F_H}^2 + {F_V}^2}}{\rho n^2 D^4}, \tag{3.2}$$

where a rotational velocity nD is used as the reference velocity, and D^2 is used as the reference area in this normalization. Hereafter, $\langle K \rangle$ denotes mean value, and $\sigma(K)$ denotes standard deviation.

Table 2 compares statistics of the unsteady loads from the coarse and fine grids to experimental results. The computed values of mean K_T and K_Q show reasonable agreement between the two grids and lie within the values measured by the water tunnel and open water experiments. An indication of experimental uncertainty is provided by the scatter observed in measured data in figure 24. The standard deviations of thrust and torque coefficients show reasonable agreement with each other and with experiment. The side-force magnitude shows larger difference between both grids, with the fine grid being closer to experiment.

Time histories of K_T, K_Q, and K_S from the fine grid are shown in figures 5(*a*)–5(*c*), respectively. The time histories show large fluctuations and low-frequency oscillations in the blade loading. The horizontal lines in figure 5 denote mean value and mean $\pm$

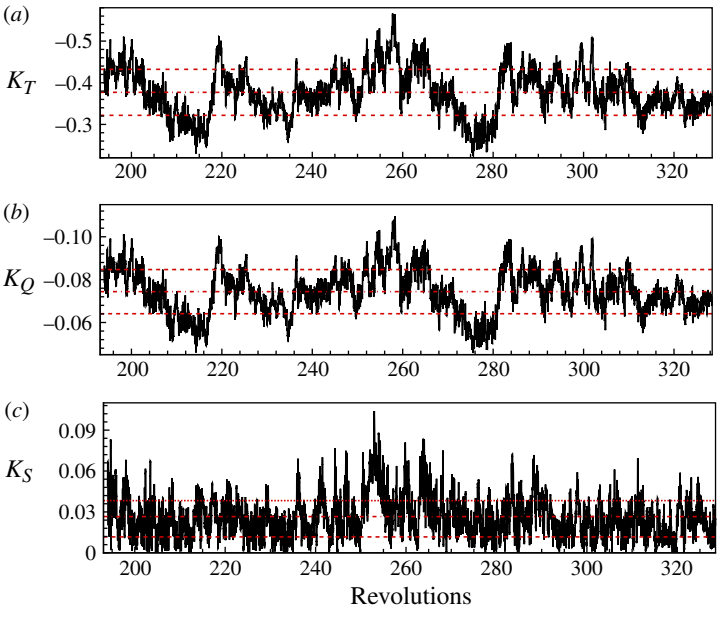

FIGURE 5. (Colour online) Time histories of unsteady loads at $J = -0.7$: (*a*) thrust coefficient K_T, (*b*) torque coefficient K_Q, (*c*) side-force coefficient K_S. Lines: ———, unsteady load; —·—, mean; – – – –, mean ± r.m.s.

	$\langle K_T \rangle$	$\sigma(K_T)$	$\langle K_Q \rangle$	$\sigma(K_Q)$	$\langle K_S \rangle$
LES (coarse)	−0.39	0.062	−0.078	0.012	0.035
LES (fine)	−0.38	0.055	−0.074	0.010	0.027
WT	−0.33	0.060	−0.065	0.011	0.030
OW	−0.41	—	−0.078	—	—

TABLE 2. Statistics of unsteady loads at $J = -0.7$.

the standard deviation. '$K > \langle K \rangle + \text{sign}(K)\sigma(K)$' is considered to be a 'high-amplitude' event, while '$K < \langle K \rangle - \text{sign}(K)\sigma(K)$' is a 'low-amplitude' event. Note that K_T and K_Q show very similar trends in figure 5(*a*,*b*). A low K_T event is observed at 215.4 rev, and a high K_T event is observed at 258.3 rev. Low- and high-amplitude events also occur in K_S around the same instant. These low- and high-amplitude events will be discussed in more detail in §§ 3.4.1 and 3.4.2.

The power spectral density (PSD) of the thrust and side-force are compared between coarse and fine grids, and to experiment in figure 6. The spectra are computed by dividing the time histories into a finite number of segments with 50 % overlap. The Hann window is applied to each segment to ensure low aliasing error and to maintain the input signal energy. The PSD is obtained as an average of the spectra over all segments. The spectra show very good agreement between coarse and fine grids and the K_T spectra are separately plotted in figure 6(*a*) for clarity. The fine grid spectra are compared to experiment in figure 6(*b*,*c*). Reasonable agreement is observed over approximately three orders of magnitude decay and two and a half decades in

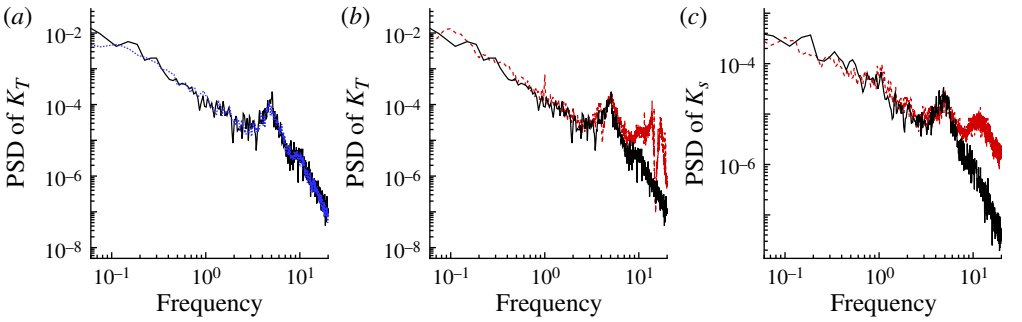

FIGURE 6. (Colour online) Power spectral density (PSD) of unsteady loads at $J = -0.7$: (*a*) grid-sensitivity study for PSD of K_T, (*b*) PSD of K_T compared to WT experiment, (*c*) PSD of K_S compared to WT experiment. Lines: ———, LES (fine); · · · · · ·, LES (coarse); – – – –, WT.

frequency. The area under the spectra being their standard deviations, this agreement is consistent with the agreement in the standard deviations of the loads observed in table 2. The computed spectra deviate from experiment for $f > 10$ (rev^{-1}). The computational time step corresponds to a frequency $f = 2.8 \times 10^3$ (rev^{-1}) which is much higher than the highest measured frequencies. The discrepancy in the PSD is therefore not likely to be due to inadequate temporal resolution. The observed agreement between spectra computed on coarse and fine grids suggests that the differences are not likely to be due to spatial discretization or grid cut-off. While the exact reasons for the difference are not known, Jessup (private communication) suggests that the differences at high frequency could occur due to blade bending and vibrations, or other shaft-related resonances affecting the measured data.

Overall, the spectra are broadband and show noticeable peaks at the blade passage frequency $f = 5$ (rev^{-1}). The loads have appreciable low-frequency content, which impacts vessel manoeuvrability. Another noticeable peak is observed in very low-frequency content, which might be related to the vortex ring shedding. The shedding frequency from WT experiment is around 0.1 (rev^{-1}), and that from LES is about 0.15 (rev^{-1}).

3.1.2. *Circumferentially averaged flow field*

The experiments provide time-averaged LDV data of the velocity field in the x–r plane in the stationary frame of reference. The time-averaged velocities from the LES are averaged over the circumferential direction and compared to experiment. Contours of the three components of mean velocity and TKE are compared in figure 7. The LES results correspond to the fine grid and the TKE is that resolved on the grid. Also, the blanked out zone corresponds to the location of propeller blades and shaft during rotation. Overall, the contours from LES and experiments look very similar. The mean axial velocity (figure 7*a*,*d*) shows that the strong reverse flow induced by the propeller rotation interacts with the surrounding free stream to create the vortex ring structure. Large radially outward flow is observed over the blades and upstream of the propeller in figure 7(*b*,*e*). Figure 7(*c*,*f*) shows that since the propeller rotates anticlockwise, the tangential velocity is primarily negative; also, the tangential velocity is especially negative upstream of the propeller.

Comparison of profiles provides a more stringent evaluation of simulation fidelity. Profiles of the circumferentially averaged velocity and TKE fields are extracted from the contour plots at five x locations; two upstream of the propeller ($x/R = -0.39$

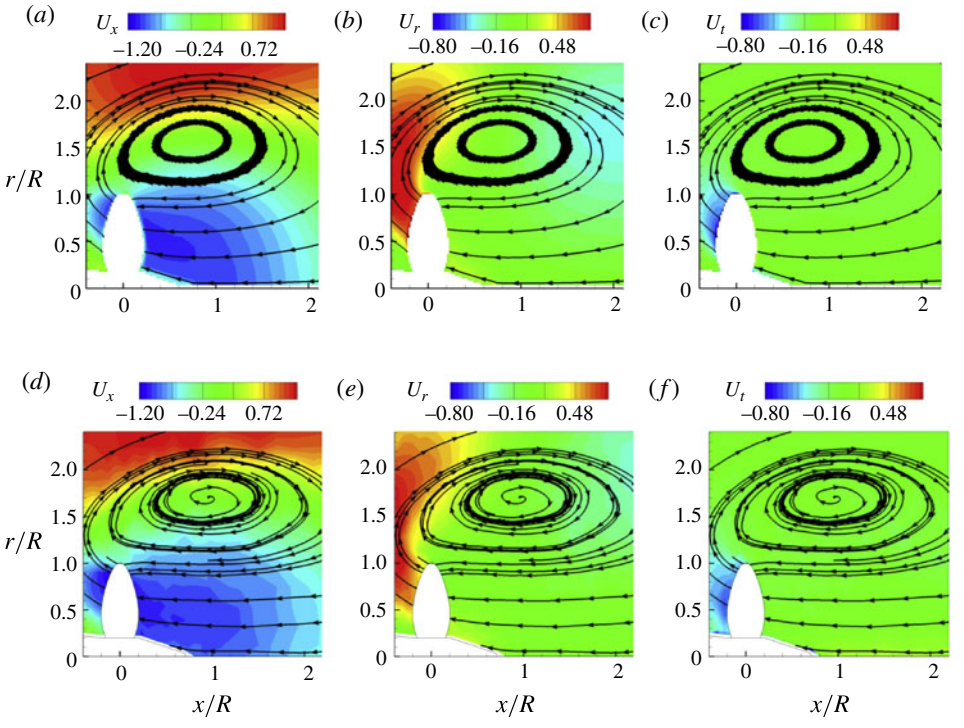

FIGURE 7. (Colour online) Circumferentially averaged flow field: (*a–c*) LES, (*d–f*) WT; (*a,d*) axial velocity, (*b,e*) radial velocity, (*c,f*) tangential velocity.

and -0.25), and three downstream of the propeller ($x/R = 0.25$, 0.50 and 0.75). Note that some of these stations pass through the vortex ring. Figure 8 compares the profiles from the coarse and fine grid LES to each other and to the WT experiment. All three components of mean velocity show encouraging agreement between the two grids and with experiment, with the fine grid results being closer to experiment in the case of differences between the grids. The resolved TKE from LES is compared to the measured TKE from the WT experiment in figure 9(*a,b*). Note that the resolved TKE shows reasonable agreement with the measured TKE, showing that most of the TKE is resolved on the grid. Apart from the observed agreement between coarse and fine grids, the fact that the resolved TKE is close to the experimental TKE offers further support that the spatial resolution captures most of the energy-containing motions.

Note that the axial velocity is opposite to the direction of the free stream at all locations in figure 8(*a*) except very near the shaft wall upstream of the propeller. This near-wall forward velocity plays an important role in determining the overall behaviour and will be discussed later. The highest levels of resolved TKE are observed in the vortex ring core region in figure 8(*d*) due to high levels of unsteadiness in the vortex ring region. Figure 9(*c*) shows the influence of the subgrid-scale (SGS) model. The maximum value of ν_t/ν is about 190 in the far-wake region, and the levels of the SGS viscosity are a little lower in the tetrahedral region. This variation is due to the different grid filter scale, $\Delta = 2\sqrt[3]{V_{cv}}$ where V_{cv} is the volume of the cell. The filter scale is vastly different between the tetrahedral region and strongly stretched prism region.

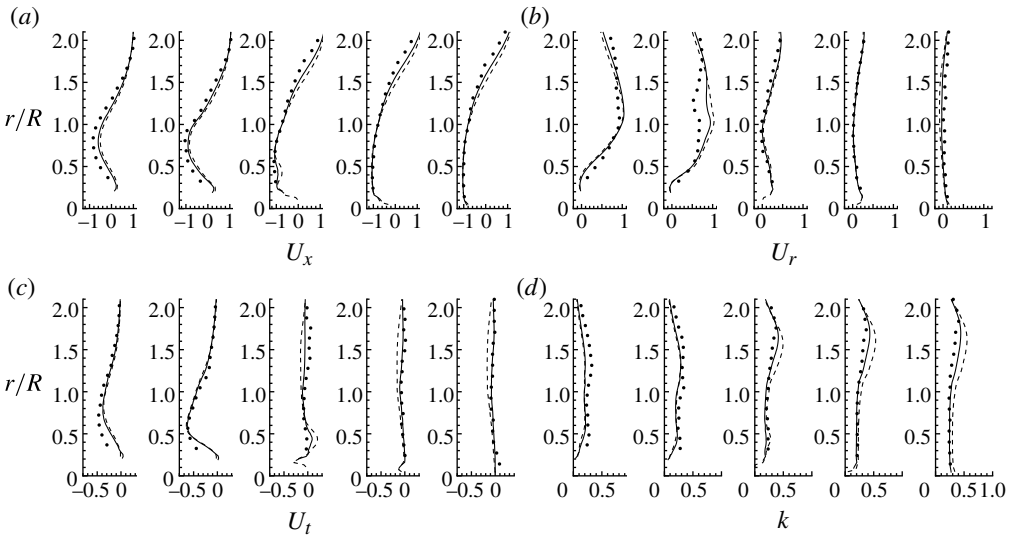

FIGURE 8. Profiles from circumferentially averaged flow field at $J = -0.7$: (a) axial velocity, (b) radial velocity, (c) tangential velocity, (d) turbulent kinetic energy. Locations of profiles are $x/R = -0.39$, $x/R = -0.25$, $x/R = 0.25$, $x/R = 0.50$, and $x/R = 0.75$, respectively. Lines: ———, LES (fine); – – – –, LES (coarse); –●–, WT.

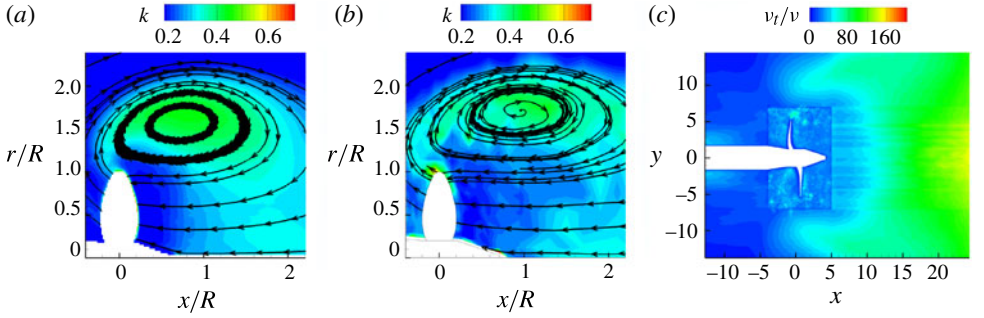

FIGURE 9. (Colour online) (a) Resolved TKE (LES), (b) measured TKE (WT), (c) effect of the SGS model; non-dimensionalized subgrid-scale eddy viscosity (ν_t/ν)).

In summary, the overall agreement between LES and experiments of Jessup *et al.* (2004) is good, and results of the grid sensitivity study are encouraging. The spatial grid adequately represents the essential flow physics near the propeller blades and the unsteady vortex ring for this massively separated flow. In what follows, the time-averaged and instantaneous flow fields from the fine-grid LES will be used to analyse the flow physics of crashback.

3.2. *Physical nature of flow in crashback*

The flow field is described in terms of its global behaviour (features on the scale of the propeller disk) and local behaviour (features in the blade passages).

3.2.1. *Global flow structure: vortex ring*

The experiments of Jiang *et al.* (1997) and Jessup *et al.* (2004, 2006) show the prominent presence of a highly unsteady vortex ring in the vicinity of the propeller

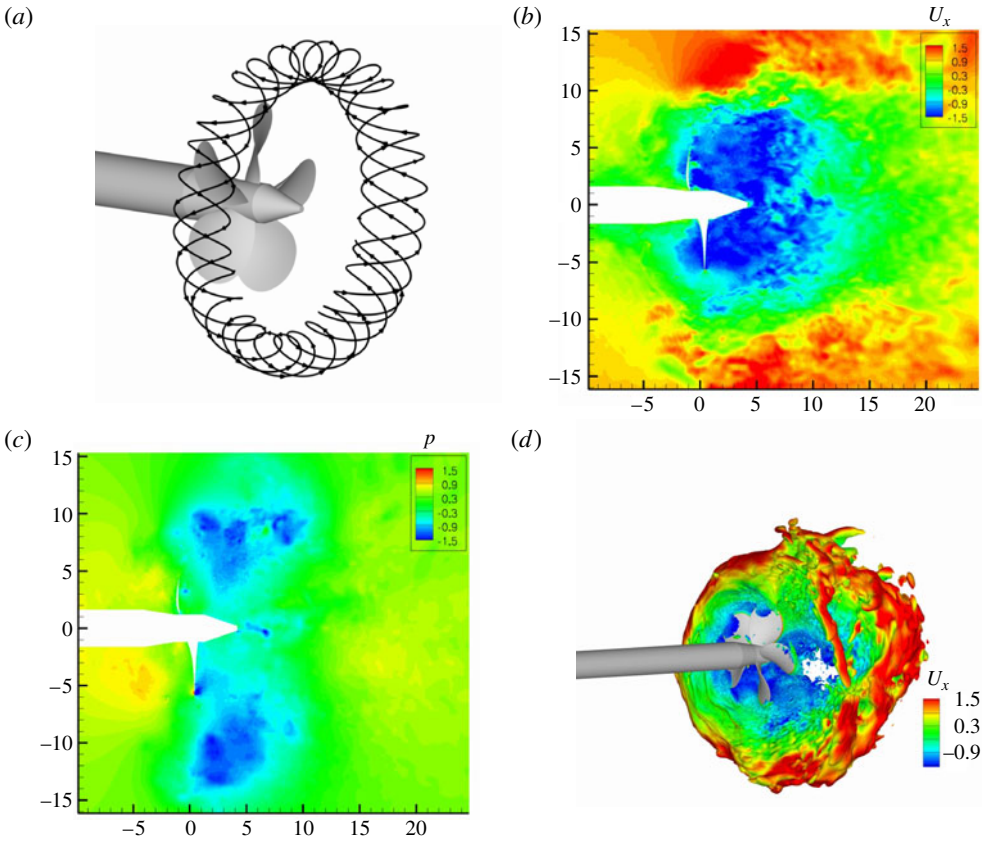

FIGURE 10. (Colour online) Unsteady vortex ring shown in (*a*) time-averaged streamlines, (*b*) instantaneous axial velocity, (*c*) instantaneous pressure, (*d*) instantaneous iso-contour of pressure ($C_p = -0.5$) coloured by axial velocity.

disk. Figure 10 shows the presence of a similar vortex ring in the LES results. The three-dimensional time-averaged streamlines in figure 10(*a*) show negative tangential velocity, indicating that the vortex ring rotates in the same direction as the propeller. Instantaneously, the vortex ring is quite irregular, as expected. In figure 10(*b*), the free stream is from left to right while the propeller rotation pushes flow through the propeller disk from right to left. The interaction between the free stream and the reverse flow induced by propeller rotation creates a recirculation zone, which is related to the vortex ring. The instantaneous pressure field in figure 10(*c*) shows the low-pressure region in the core of the vortex ring, and the three-dimensional structure of the vortex ring is visualized using an iso-surface of constant low pressure in figure 10(*d*). Vortex rings are unstable at high Reynolds numbers; as a result the ring sheds at irregular intervals. Such shedding influences the high transient loads on the propeller, and is further discussed in § 3.4.2. No definite shedding frequency of the vortex ring is observed, as noted in Jessup *et al.* (2004).

Vortex rings have been studied by many researchers (see e.g. the review of Shariff & Leonard 1992), but most work has focused on the formation and evolution of vortex rings created by pulsed jets. The interaction of the reverse flow through the propeller disk with the free stream may be idealized as a round jet in counterflow, which has

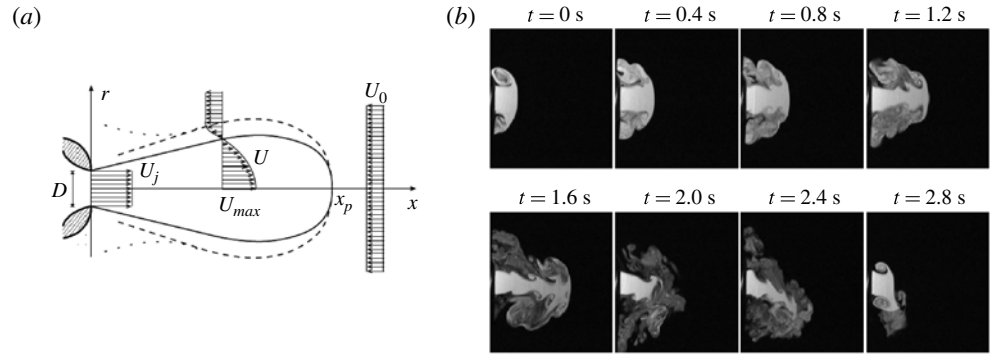

FIGURE 11. (*a*) Schematic of a jet in counterflow, (*b*) time evolution of vortex ring for a jet in counter flow at $\alpha = 1.3$ (reprinted with permission from Bernero, PhD thesis, Technische Universität Berlin, 2000).

been studied experimentally (e.g. Yoda & Fiedler 1996; Bernero 2000). A schematic of a jet in counterflow is shown in figure 11(*a*); note that the jet velocity U_j is opposite to the counterflow velocity U_0. The qualitative nature of the flow depends on the velocity ratio $\alpha = U_j/|U_0|$. For low α, an axisymmetric vortex ring is formed and shed regularly; this regime is termed the 'stable case'. On the other hand, above a certain α the jet tip appears to exhibit low-frequency oscillations and is termed the 'unstable case'. Figure 11(*b*) shows experimental visualization of the vortex ring for jet in counterflow at a critical velocity ratio ($\alpha = 1.3$). Note that an axisymmetric vortex ring is created at the beginning (stable), and becomes asymmetric and flaps (unstable) as time evolves. The cycle appears to restart with the stable case at $t = 2.8$ s. No regular shedding or cycle frequency has been observed due to the extreme sensitivity of the flow to small perturbations (Bernero 2000).

A similar flow has been computationally studied using an unsteady actuator disk model by Vyšohlid & Mahesh (2007). A schematic of the actuator disk model is shown in figure 12(*a*); note that the actuator disk enforces constant flow velocity U_P against the free-stream velocity U. Vyšohlid & Mahesh (2007) performed simulations at $U_P/U = -1.0$ and noted regular vortex ring shedding. Figure 12(*b–e*) from Vyšohlid & Mahesh (2007) shows the evolution of the vortex ring in time. A new vortex ring is created around the actuator disk (*b*), advected with the free stream (*c*), stretched (*d*), and shed (*e*). The counterflowing jet and actuator disk visualizations suggest that the vortex ring in crashback may be considered to result from the reverse flow induced by propeller rotation interacting with the free stream.

3.2.2. *Local flow structure: LE separation on blade*

The vortex ring may be considered a global feature of the crashback flow. In this section, the local flow structure in the blade passages is studied. Figure 13 shows the time-averaged axial velocity and pressure at the centre of the propeller disk ($x/R = 0$). Note that the axial velocity over most of the blade passage (figure 13*a*) is negative (opposite to the free-stream direction) with magnitudes approaching 1.5 times the free-stream velocity. As observed earlier, the axial velocity is positive over a small region near the blade root; note that the magnitudes approach the free-stream value. As a result, mass flow across the tunnel cross-section is conserved by fluid accelerating around the propeller disk over the vortex ring. The mean pressure difference across the

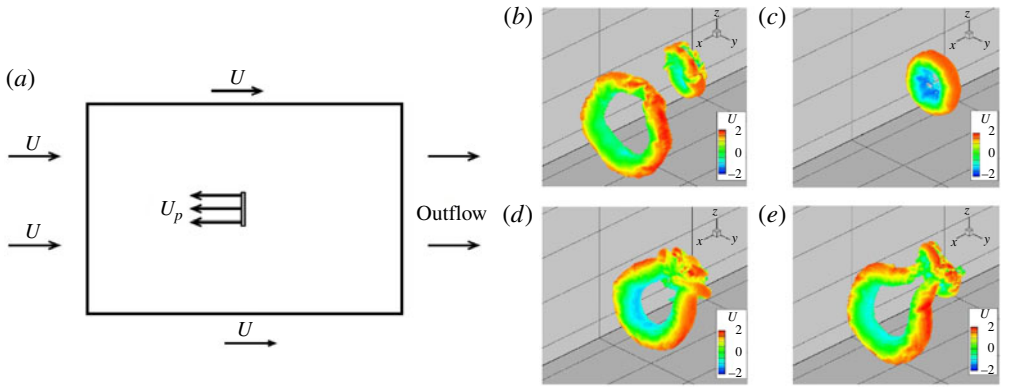

FIGURE 12. (Colour online) (*a*) Schematic of the actuator disk model, (*b–e*) time evolution of vortex ring in the actuator disk model at $U_P/U = -1.0$ (Vyšohlid & Mahesh 2007).

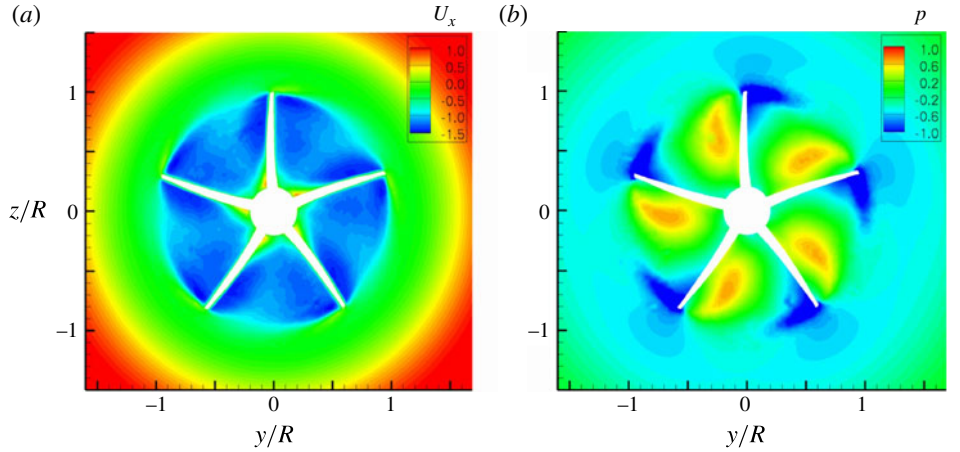

FIGURE 13. (Colour online) Time-averaged flow field at $x/R = 0$ and $J = -0.7$: (*a*) axial velocity, (*b*) pressure.

propeller blades is higher near the blade tips; also the pressure and suction sides in crashback are opposite to those in the forward mode.

Figure 14 shows the mean and r.m.s. values of pressure, mean axial velocity and streamlines inside the blade passages at a constant radius ($r = 0.4R$). Recall that the sharp trailing edge (TE) of the forward mode becomes the leading edge (LE) with respect to the local flow in crashback. The velocity vector is transformed to the rotating frame of reference to obtain streamlines over the blade sections relative to the blade. The velocity in the fixed frame ($\boldsymbol{U}$) and the velocity in the rotating frame ($\boldsymbol{V}$) are related as follows:

$$\boldsymbol{U} = \boldsymbol{u}_x + \boldsymbol{u}_r + \boldsymbol{u}_\theta, \tag{3.3a}$$

$$\boldsymbol{V} = \boldsymbol{u}_x + \boldsymbol{u}_r + (\boldsymbol{u}_\theta - \boldsymbol{\omega} \times \boldsymbol{r}). \tag{3.3b}$$

Figure 14(*a*) shows pressure contours with streamlines in the rotating frame. Note the large pressure difference near the sharp leading edge similar to 'leading edge

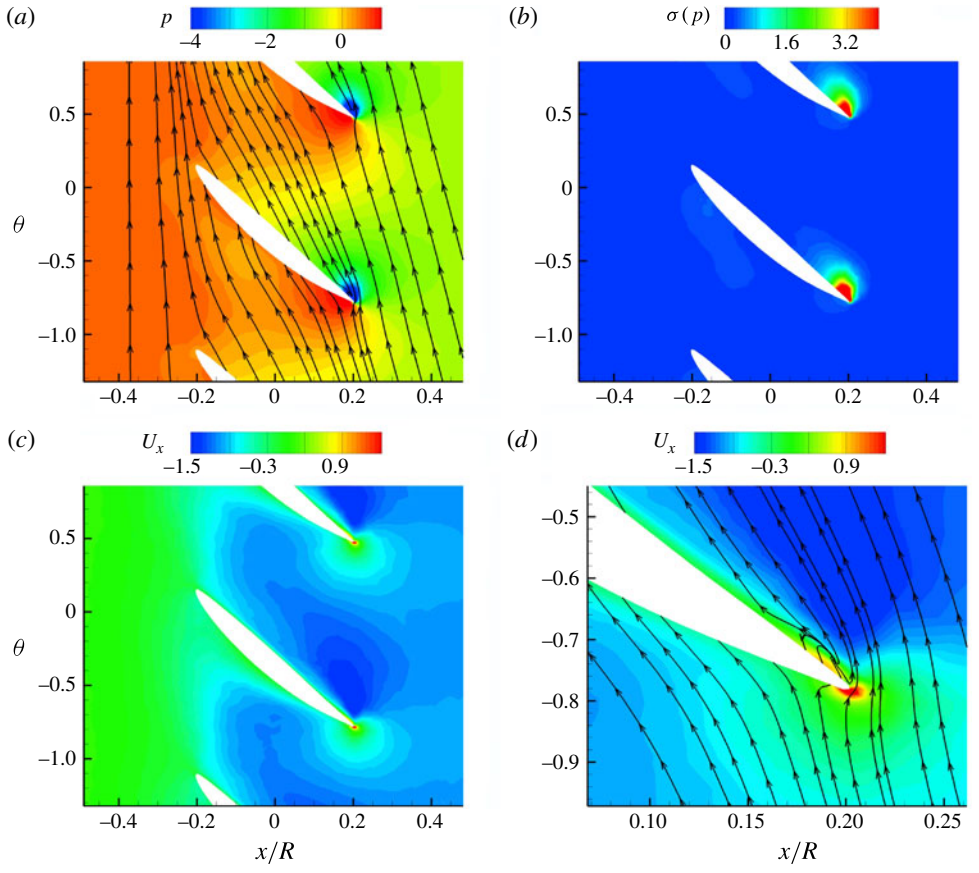

FIGURE 14. (Colour online) Time-averaged flow field in the blade passage at $r = 0.4R$ and $J = -0.7$: (*a*) pressure with streamlines, (*b*) r.m.s. of pressure, (*c*) axial velocity, (*d*) axial velocity with streamlines at leading edge.

suction' observed in conventional aerofoils. However, the pressure and suction sides are opposite to that in the forward mode. The pressure field near the leading edge is highly unsteady as indicated by contours of the r.m.s. pressure in figure 14(*b*). This unsteadiness will manifest itself in the propeller loads being unsteady. Close examination of the axial velocity at the LE in figure 14(*d*) shows the unsteadiness to be associated with the recirculation region formed when the flow separates. This separation is a result of the reverse flow incident at high angle of attack at the sharp leading edge. As shown in figure 14(*c*), the mean axial velocity is negative over most of the blade passage.

The three-dimensional complexity of the flow is illustrated in figure 15, which shows time-averaged streamlines with pressure contours on blade surfaces. The streamlines plotted on the blade surfaces are obtained at the centroid of the first grid cell. On the hub surface ($r = 0.2R$), two flow separations are observed both at LE and TE. While the LE separation is a prominent feature as shown in figure 14, the TE separation is a result of the forward velocity near the hub mentioned in § 3.1.2 and shown in figure 8, impinging on the blade near the pressure side TE. Both LE and TE recirculation regions interact at the middle of the suction side near the root to

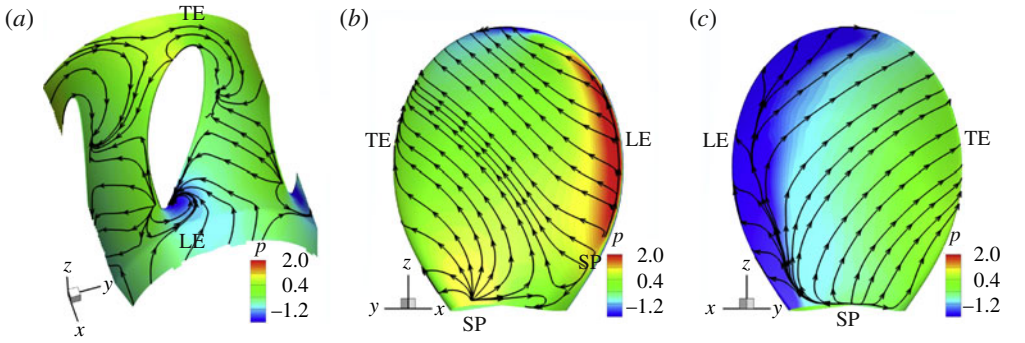

FIGURE 15. (Colour online) Time-averaged streamlines with pressure contours on propeller surface at $J = -0.7$: (*a*) on the hub, (*b*) on the pressure side, (*c*) on the suction side.

produce a stagnation point there, and radially outward flow. Note that LE separation is observed along the entire LE, while the TE separation is restricted to the blade root region. Overall, the fluid on both sides of the blade flows in the radially outward and upstream directions. In particular, the fluid at the LE flows radially outward along the LE.

3.3. *Spatial variation of blade loads*

The individual contributions of pressure and viscous forces to thrust and side-force are shown in table 3. Note that viscous force is much smaller than pressure force due to the high Reynolds number and the flow being massively separated. This behaviour is consistent with the Reynolds number insensitivity observed by Jessup *et al.* (2004) for $Re > 400\,000$. The pressure field therefore provides a good measure of the blade loading. However, since the local blade normals are not necessarily aligned with either the thrust or the side-force, their contribution to the thrust and side-force cannot be assessed from pressure alone. An effective pressure is therefore defined below to account for the contribution of local blade orientation to the loads. We define unit thrust δT and side-force magnitude δS on a unit surface as follows:

$$\delta T = \delta \boldsymbol{F} \cdot \boldsymbol{i} = p\,(\boldsymbol{n}_f \cdot \boldsymbol{i}) \equiv p\,\alpha_f, \tag{3.4a}$$

$$\delta S = \sqrt{(\delta \boldsymbol{F} \cdot \boldsymbol{j})^2 + (\delta \boldsymbol{F} \cdot \boldsymbol{k})^2} = |p| \sqrt{(\boldsymbol{n}_f \cdot \boldsymbol{j})^2 + (\boldsymbol{n}_f \cdot \boldsymbol{k})^2} \equiv |p|\,\beta_f \tag{3.4b}$$

where p is the pressure, $\boldsymbol{n}_f$ is the outward normal vector of the face, and $\boldsymbol{i}, \boldsymbol{j}, \boldsymbol{k}$ are unit vectors. $p\,\alpha_f$ and $|p|\,\beta_f$ determine the local pressure contribution to thrust and side-force, and are termed the 'effective pressure' for thrust and side-force, respectively. It is easily seen that the geometric quantities α_f and β_f are invariant with rotation so that they are compatible with the rotating co-ordinate system. The mean value of effective pressure for thrust is obtained as

$$\langle \delta T \rangle = \langle p \rangle\, \alpha_f. \tag{3.5}$$

Since mean values of F_H and F_V are theoretically zero, $\sqrt{\langle \delta S^2 \rangle}$ is obtained as

$$\sqrt{\langle \delta S^2 \rangle} = \sqrt{\sigma^2(F_H) + \sigma^2(F_V)} = \sigma(p)\,\beta_f. \tag{3.6}$$

Equations (3.5) and (3.6) describe how different parts of the blade contribute to the thrust and side-forces. Contours of $\langle \delta T \rangle$ on the pressure and suction sides are shown

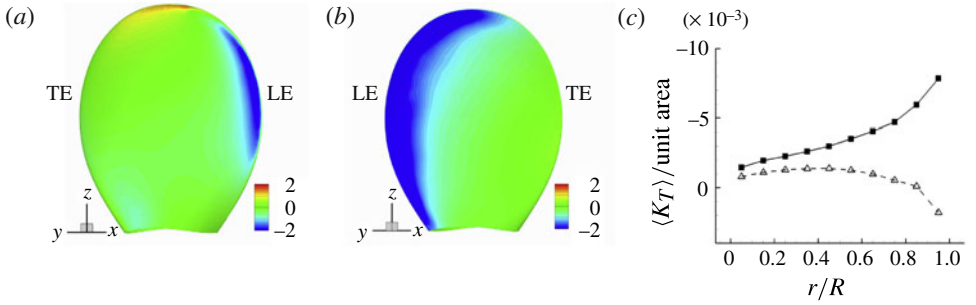

FIGURE 16. (Colour online) Thrust distribution on the blade at $J = -0.7$: (*a*) effective pressure for thrust on the pressure side, (*b*) effective pressure for thrust on the suction side, (*c*) $\langle K_T \rangle$ on the unit surface area for radially divided sections. ■, suction side; △, pressure side.

$\langle K_T \rangle$	$\langle K_{Tp} \rangle$	$\langle K_{Tv} \rangle$	$\langle K_S \rangle$	$\langle K_{Sp} \rangle$	$\langle K_{Sv} \rangle$
-3.77×10^{-1}	-3.77×10^{-1}	3.40×10^{-4}	2.70×10^{-2}	2.70×10^{-2}	7.61×10^{-5}

TABLE 3. Components of mean coefficients of thrust and side-force at $J = -0.7$; p and v denote the pressure and viscous contribution respectively.

in figure 16(*a,b*). The integral of $\langle \delta T \rangle$ over both surfaces corresponds to the net thrust. Note that most of the thrust originates from the sharp leading edge where the flow is separated and unsteady (§ 3.2.2). The radial distribution of the loads is characterized by dividing the blade into ten radial strips, integrating the effective pressures over each strip, and dividing by the area of each strip. As shown in figure 16(*c*), such normalized thrust is highest near the blade tips. The physical reason for this behaviour is the higher angle of attack induced by the vortex ring at the blade tip. Similar behaviour is observed for the side-force (figure 17) in that the leading edge of the suction side contributes the most. Interestingly, a small portion near the blade's trailing edge close to the root experiences discernible levels of side-force. Recall from § 3.2.2 that flow separates at the trailing edge in this region.

3.4. *Flow physics during extreme loading events*

As shown in figure 5, the instantaneous loads in crashback can be much higher or lower than their mean values. K_T, for example, varies between 0.6 and 1.5 of its mean value. This section uses the conditional-averaging technique (Antonia 1981) to quantitatively describe the statistically relevant events that determine low- and high-amplitude thrust and side-forces. Also, the instantaneous flow fields corresponding to extreme loading events are discussed.

3.4.1. *Conditional averages for thrust and side-force*

First, mean values and standard deviations of K_T and K_S are estimated *a priori* from the previously computed time histories. High-amplitude events are defined as those where K is higher than $\langle K \rangle + 1.5\,\mathrm{sign}(K)\,\sigma(K)$, and low-amplitude events are when K is less than $\langle K \rangle - 1.5\,\mathrm{sign}(K)\,\sigma(K)$. Here K denotes K_T or K_S. The conditional averaging is performed over 135 revolutions.

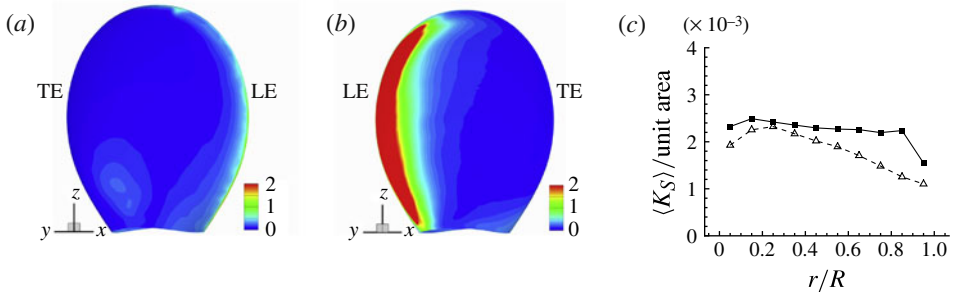

FIGURE 17. (Colour online) Side-force distribution on the blade at $J = -0.7$: (*a*) effective pressure for side-force on the pressure side, (*b*) effective pressure for side-force on the suction side, (*c*) $\langle K_S \rangle$ on the unit surface area for radially divided sections. ■, suction side; △, pressure side.

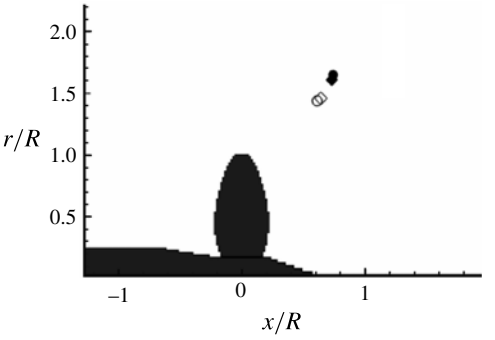

FIGURE 18. The locations of conditionally averaged vortex ring cores at $J = -0.7$: ⧫, low K_S; ◇, high K_S; •, low K_T; ○, high K_T.

The locations of vortex ring cores, and profiles of mean axial velocity and resolved turbulent kinetic energy (TKE), are shown in figures 18 and 19 to illustrate the global behaviour of the flow during extreme K_T and K_S events. The vortex ring is noticeably closer to the propeller disk when the loads are high (figure 18). Also, figure 19(*b,d*) show that during high-amplitude events, the resolved TKE is significantly higher at all locations, especially in the region of the vortex ring core. The flow is therefore increasingly unsteady when the loads are high; as will be seen in § 3.4.2 these instants correspond to higher levels of blade passage separation, and vortex ring formation and break-up.

The conditionally averaged profiles in figure 19 show that the flow is qualitatively similar during low- and high-amplitude events for K_T and K_S. The profiles of resolved TKE conditioned on K_T and K_S are quite similar while the mean velocity conditioned on K_S events shows smaller differences than that conditioned on K_T. This behaviour is consistent with the fact that mean side-force is zero due to mean axisymmetry of the flow; the side-force only has a fluctuating component. This similarity in the conditionally averaged profiles suggests that the dominant flow physics that yield extreme thrust and side-force events are similar. The correlation between thrust and side-force events is quantitatively represented by the correlation coefficient between K_T and K_S. The correlation coefficient between K_T and K_S is -0.32 during the entire

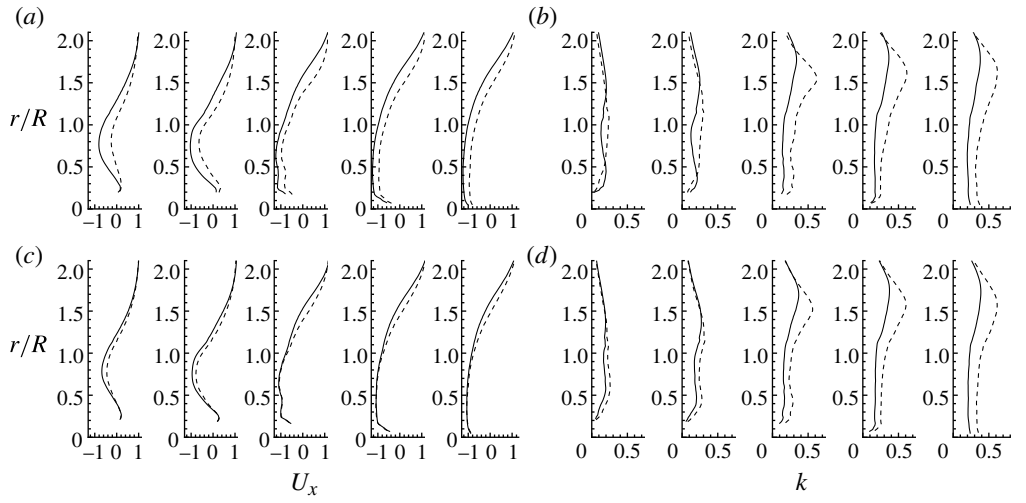

FIGURE 19. Profiles from the conditionally averaged flow field at $J = -0.7$: (a,b) K_T events, (c,d) K_S events; (a,c) axial velocity, (b,d) TKE. Locations of profiles are $x/R = -0.39$, $x/R = -0.25$, $x/R = 0.25$, $x/R = 0.50$, and $x/R = 0.75$, respectively. Lines: ———, low-amplitude events; – – – –, high-amplitude events.

period. Also, the correlation is stronger during high-amplitude events and weaker during low-amplitude events.

The mean axial flow is different during high- and low-amplitude events. Stronger reverse axial flow is consistently observed at all locations during low K_T events in figure 19(a). On the other hand, the forward velocity near the shaft wall is stronger during high K_T events. Flow separation in the blade passages is affected as a result. Conditionally averaged streamlines and pressure on the blade surfaces are shown in figure 20. Note from figure 20a,d that both LE and TE separations are much stronger during high K_T events than low K_T events. Recall that the forward velocity near the hub due to the free-stream momentum causes TE separation and exacerbates LE separation in § 3.2.2. Thus, stronger LE and TE separations are a result of the higher forward velocity. The higher forward flow impinges on the blade near the pressure side TE and causes a high-pressure region there during high K_T events in figure 20(e). During high K_T events, LE and TE recirculation regions interact at the middle of the suction side and produce radially outward flow in figure 20(f). Overall, the fluid on the suction side flows in the radially outward direction during high K_T events, and flows upstream during low K_T events.

3.4.2. *Instantaneous flow fields at extreme events*

This section compares instantaneous flow fields at low- and high-amplitude events. As seen from figure 5, the flow at 215.4 rev and 258.3 rev corresponds to low and high propeller loads respectively. Pressure contours in the x–y plane and three-dimensional iso-contours of pressure (figure 21) reveal a more coherent vortex ring when the load amplitudes are low; the ring breaks up and sheds when the loads are high. Also note that when the loads are high, a smaller vortex ring is observed closer to the propeller. Figure 21(c,f) compares axial velocities during low- and high-amplitude events. Note that the reverse flow is noticeably stronger when the loads are low, and higher forward velocities are observed at the root of the propeller when

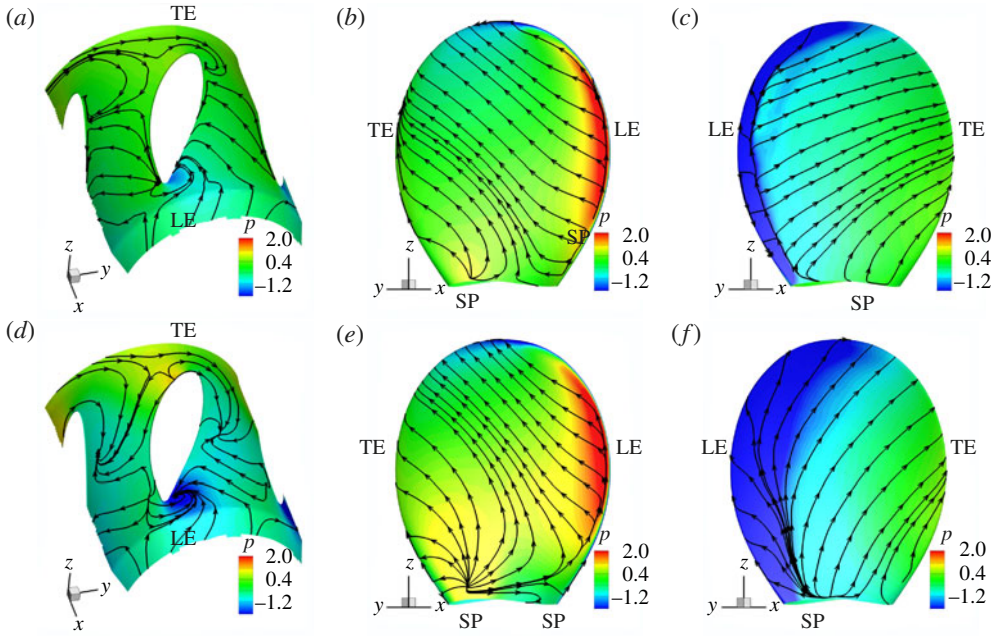

FIGURE 20. (Colour online) Streamlines with pressure contours of conditionally averaged flow field at $J = -0.7$: (*a–c*) low K_T events, (*d–f*) high K_T events; (*a,d*) on the hub, (*b,e*) on the pressure side, (*c,f*) on the suction side.

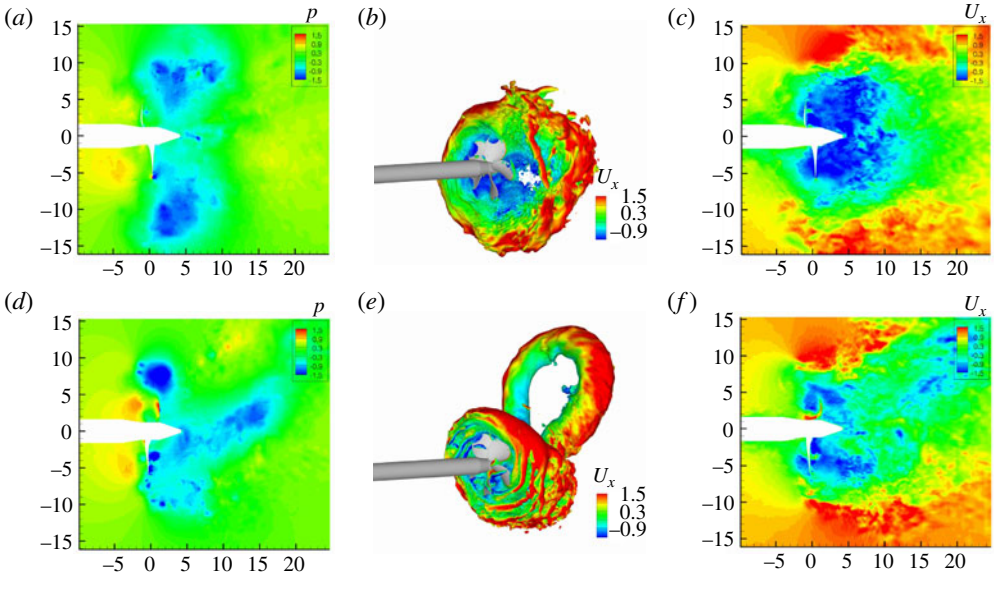

FIGURE 21. (Colour online) Comparison of instantaneous flow fields at $J = -0.7$: (*a–c*) low-amplitude events, (*d–f*) high-amplitude events; (*a,d*) pressure contour, (*b,e*) iso-contour of pressure coloured by axial velocity, (*c,f*) axial velocity.

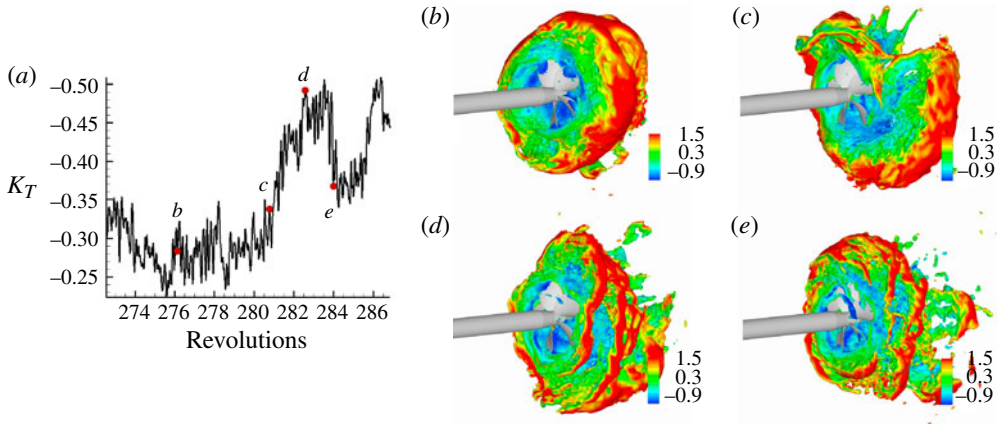

FIGURE 22. (Colour online) (*a*) Time history of K_T, (*b–e*) time evolution of vortex ring in crashback at $J = -0.7$.

the loads are high. Figure 21 does not show the time evolution of the vortex ring as shown in the actuator disk model in figure 12. The time evolution of a vortex ring in crashback is shown in figure 22 with a time history of K_T. The vortex ring is most coherent at low thrust as shown in figure 22(*b*). The coherence of the vortex ring starts to break in figure 22(*c*). The vortex ring is stretched in figure 22(*d*) at the highest thrust, and finally shed in figure 22(*e*). Even though the time evolution of the vortex ring is not as clear as in the actuator disk model, a similar tendency is observed in the figure.

Figure 23 compares instantaneous flow in the blade passages at $r/R = 0.4$. Corresponding time histories of K_T and K_S are plotted in figures 23(*a*) and 23(*c*) respectively. Low-amplitude loads are observed at 216.1 rev ('A' in the figures), and high-amplitude loads are seen at 218.4 rev ('B' in the figures). Note that the LE separation is highly unsteady and several secondary separation vortices are observed when the loads are high in figure 23(*d*). In contrast, the blade passage flow is relatively quiescent during low-amplitude events. This instantaneous behaviour is consistent with the statistical observations in § 3.4.1.

3.5. *The effect of advance ratio*

Thus far we have considered propeller crashback at $J = -0.7$ in detail. Large eddy simulations are also performed at $J = -0.5$ and $J = -1.0$ at the same Reynolds number to assess the effect of advance ratio. Since $J = U/nD$, for fixed free-stream velocity U, propeller rotation is faster at $J = -0.5$ and slower at $J = -1.0$.

3.5.1. *Magnitudes of unsteady loads*

Statistics of unsteady loads are obtained over 213.33 rev at $J = -0.5$ and over 208.33 rev at $J = -1.0$. Figure 24(*a,b*) compares the mean thrust and torque coefficients to WT and OW experimental data. The computed loads lie within experimental scatter, consistent with results for $J = -0.7$ in § 3.1.1. Note that K_T and K_Q become increasingly negative as J varies from -0.7 towards -1.2; their values show less variation over the range -0.6 to -0.2. K_T, K_Q, and K_S use propulsive scaling, i.e. they are non-dimensionalized using n and D. Since the propeller rotation rate is large for small magnitudes of J, the loads will probably scale with n and D in

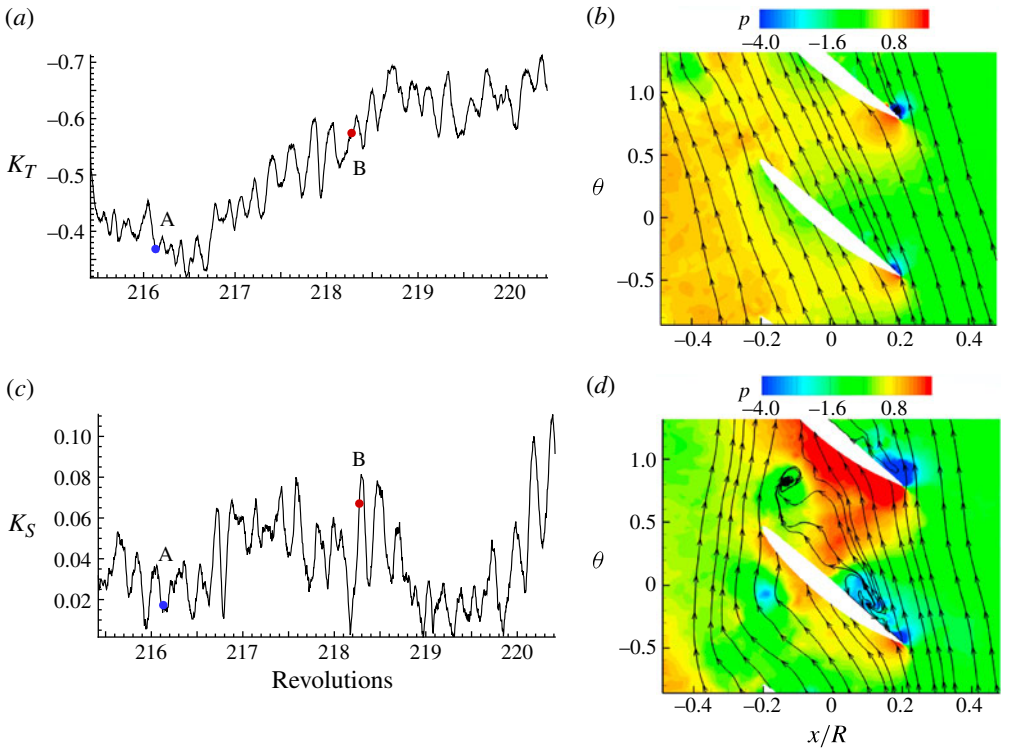

FIGURE 23. (Colour online) (*a*) Time history of K_T, (*b*) pressure with streamlines in the blade passage at a low-amplitude event, (*c*) time history of K_S, (*d*) pressure with streamlines in the blade passage at a high-amplitude event.

this regime. In contrast, the loads will probably scale with the free-stream velocity U for large magnitudes of J (where n is small). Normalizing using the dynamic pressure based on the free-stream velocity (U) yields

$$C_T = \frac{T}{\frac{1}{2}\rho U^2 A_D}, \quad C_Q = \frac{Q}{\frac{1}{2}\rho U^2 A_D D}, \quad C_S = \frac{S}{\frac{1}{2}\rho U^2 A_D}, \tag{3.7}$$

where $A_D = \pi D^2/4$ is the propeller disk area. As a result,

$$C_T = \frac{8}{\pi}\frac{K_T}{J^2}, \quad C_Q = \frac{8}{\pi}\frac{K_Q}{J^2 D}, \quad C_S = \frac{8}{\pi}\frac{K_S}{J^2}. \tag{3.8}$$

Figure 24(*c,d*) shows the variation of C_T, C_Q, and C_S with J. As suggested above, these coefficients vary slightly for large magnitudes of J and considerably for small magnitudes of J.

3.5.2. *Physical nature of flow at different advance ratios*

Figure 25 shows contours of the circumferentially averaged axial velocity and resolved TKE at both advance ratios. The mean streamlines indicate the presence of the vortex ring in the vicinity of the propeller disk. Note that the reverse flow through the propeller disk is stronger at $J = -0.5$, consistent with the higher rotation rate. Recall that the reverse flow interacts with the free stream to produce the vortex ring.

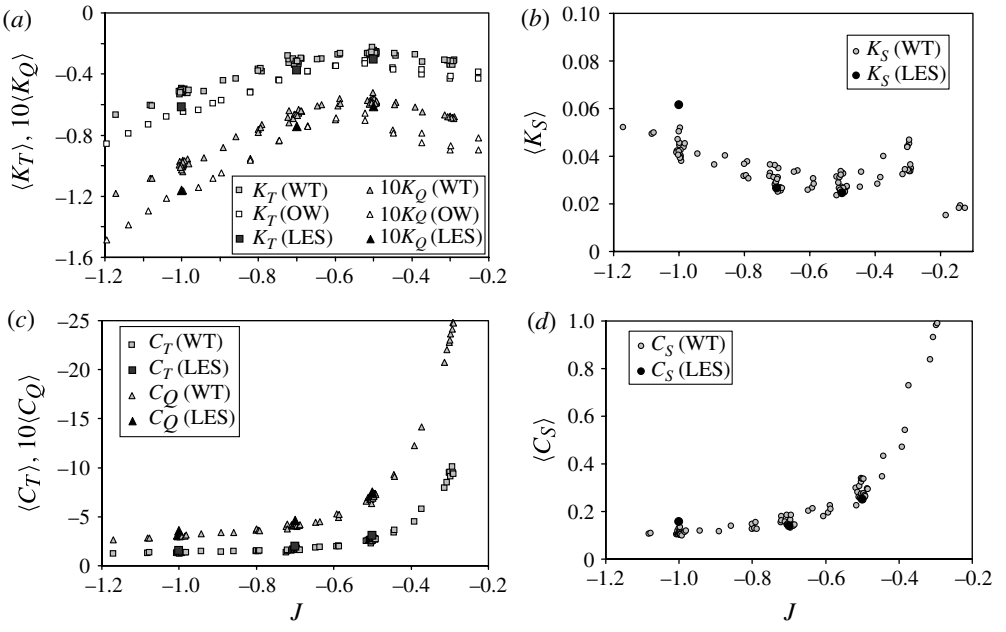

FIGURE 24. Mean unsteady loads versus advance ratio J: (*a*) K_T & K_Q, (*b*) K_S, (*c*) C_T & C_Q, (*d*) C_S. Experimental data are provided by NSWCCD.

The vortex ring is therefore closer to the propeller blades at $J = -0.5$ (figure 26*a*). The vortex ring location at $J = -0.7$ is intermediate to its location at $J = -0.5$ and -1.0. Figure 25(*b,d*) shows contours of the resolved TKE as a measure of flow unsteadiness. Overall, the TKE is higher for $J = -0.5$ as compared to $J = -1$, consistent with the higher propeller rotation rate. Also, note that the TKE at $J = -0.5$ is highest in the vortex ring due to its meandering and break-up, and near the stagnation streamline upstream of the propeller disk, where the reverse flow through the propeller and the free-stream velocities interacts.

The flow in the blade passages is correspondingly different. As the mean streamlines in figure 26(*b,c*) show, the leading edge separation is higher for $J = -1.0$ compared to that at $J = -0.5$. This behaviour is consistent with the conditionally averaged results obtained for $J = -0.7$, where it was seen that low reverse velocities yielded larger leading edge separation and high values of K_T and K_S, while high reverse velocities yielded the opposite behaviour.

4. Summary

A large body of work exists on propellers in the forward mode of operation ($U > 0$, $\omega > 0$). Significantly less is known about the equally fundamental condition of crashback, where the propeller rotates in the reverse direction ($U > 0$, $\omega < 0$). The crashback condition is most common in marine propellers; however, different aspects of the flow are also relevant to applications such as rotating stall in turbomachinery and helicopter rotors in hover. This paper uses large eddy simulation to study this massively separated flow at a Reynolds number of 480 000 and advance ratios $J = -0.5$, -0.7 and -1.0.

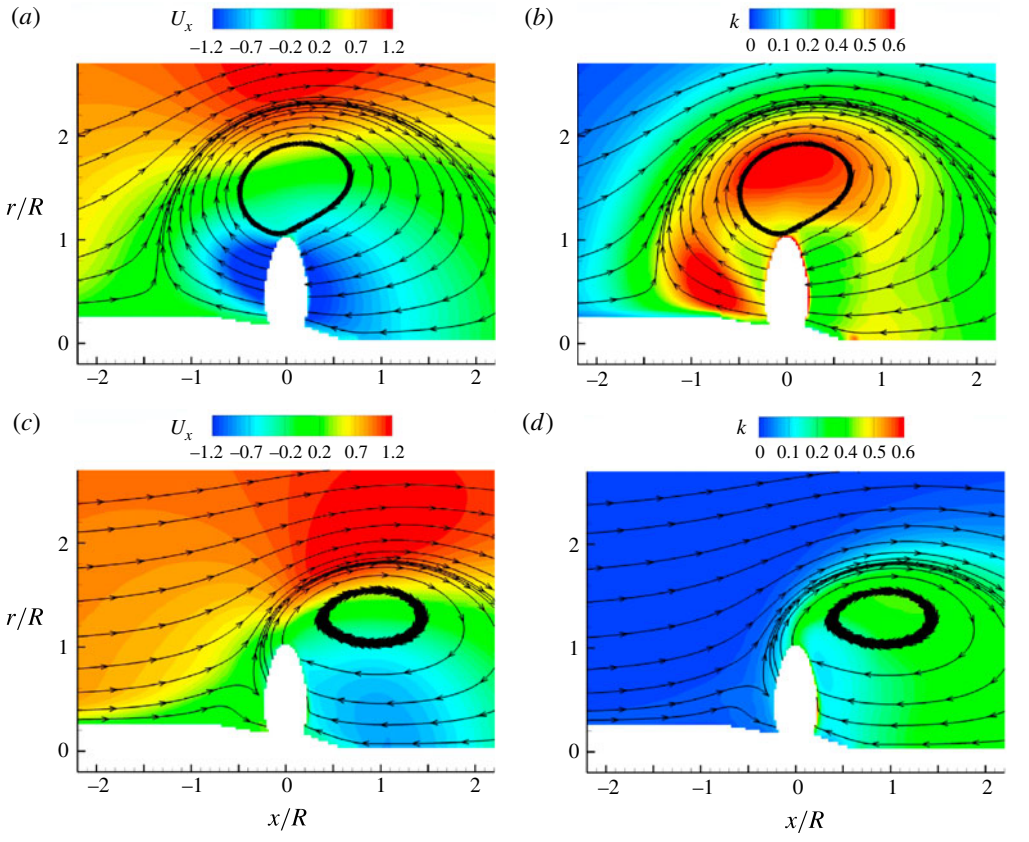

FIGURE 25. (Colour online) Circumferentially averaged flow field with streamlines at different J: (*a,b*) $J = -0.5$, (*c,d*) $J = -1.0$; (*a,c*) axial velocity, (*b,d*) TKE.

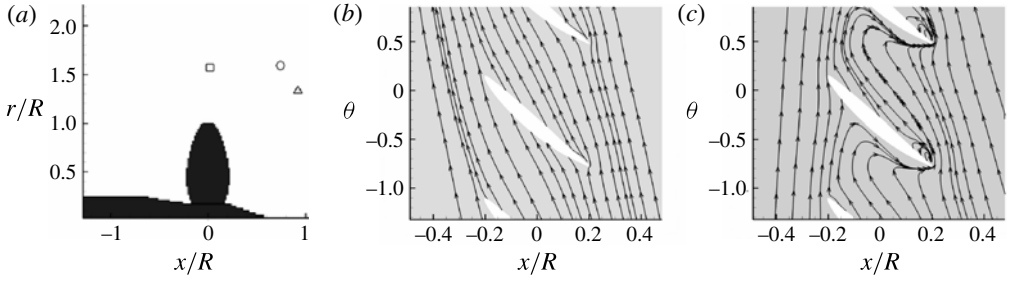

FIGURE 26. (*a*) Locations of vortex ring cores at different J: □, $J = -0.5$; ○, $J = -0.7$; △, $J = -1.0$. (*b,c*) Mean streamlines in the blade passage at $r = 0.4R$ and at (*b*) $J = -0.5$, (*c*) $J = -1.0$.

Simulations are performed on two grids of 7.7 and 19 million control volumes and the results are compared to each other and to the experiments of Jessup *et al.* (2004, 2006). The compared quantities include mean values, standard deviations and spectra of the loads, the three components of mean velocity and resolved TKE. The

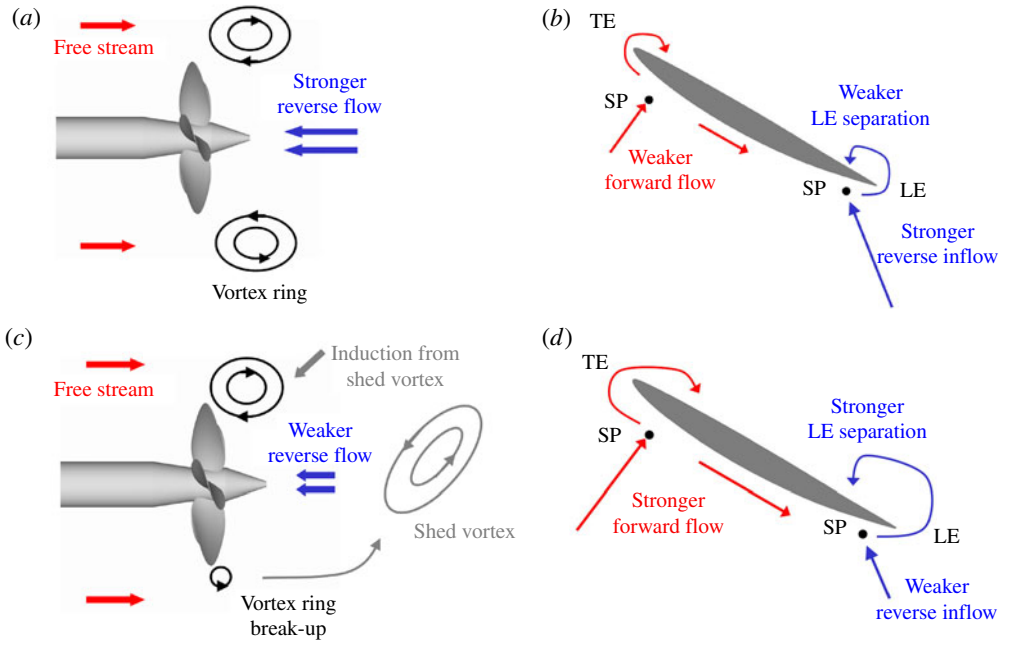

FIGURE 27. (Colour online) Schematic of flow physics in crashback: (*a*) axisymmetric vortex ring during low-amplitude events, (*b*) flow in the blade passage on the hub during low-amplitude events, (*c*) vortex ring break-up during high-amplitude events, (*d*) flow in the blade passage on the hub during high-amplitude events.

overall agreement between LES and experiment is good, and results of the grid comparison study are encouraging in that a significant fraction of the TKE is resolved by the computational grid. The subgrid eddy viscosity ranges from about 190 in the far-wake region to lower levels in the near-wake, where the computational grid is finer.

The LES results are analysed to study the physical behaviour of the flow. The flow field is described in terms of features on the scale of the propeller disk (global) and features in the blade passages (local). The global flow consists of a strong reverse flow through most of the propeller disk and a highly unsteady vortex ring in its vicinity. This behaviour may be explained as follows. The cross-section of a propeller blade is an aerofoil, and rotating in reverse is equivalent to a negative angle of attack; the pressure and suction sides are therefore interchanged. The propeller blades therefore push fluid in the reverse direction towards the free stream. The collision between these two opposing streams of fluid produces a vortex ring. A higher reverse flow (with respect to the free stream) causes the vortex ring to form closer to the propeller disk. Their inherent hydrodynamic instability results in the vortex rings being irregular and unsteady at high Reynolds numbers. Similar vortex rings are observed in visualizations of the flow in counterflowing jets and an actuator disk model.

This global flow affects the flow in the blade passages as follows. The reverse flow ensures that the leading and trailing edges are interchanged when defined with respect to the local flow. Flow separates at the sharp leading edge and is unsteady there. A large leading edge suction exists, which combines with the unsteadiness to yield large levels of pressure fluctuations at the leading edge. Such separation occurs along the entire leading edge of the blade. The leading edge separation near the blade tips is

affected by their proximity to the vortex ring and the resulting influence on the local angle of attack. Some flow separation is also observed at the trailing edge near the hub.

Predictably, the unsteady flow results in propeller loads being unsteady; e.g. K_T varies from 0.6 to 1.5 of its mean value when $J = -0.7$. The local blade normals are not necessarily aligned with either the thrust or the side-force; an effective pressure is therefore defined to account for the contribution of local blade orientation to the loads. Such analysis reveals that most of the thrust and side-force originate from the leading edge separation. Conditional averaging is used to describe the statistically relevant events that determine low- and high-amplitude thrust and side-forces. When the loads are high, the vortex ring is closer to the propeller disk and the reverse flow is weaker at the sharp leading edge, resulting in a larger LE separation. Further, high loads correspond to higher levels of unsteadiness resulting from vortex ring formation and break-up and blade passage separation.

The essential physical nature of the flow and its relation to propeller loads is schematically shown in figure 27. Also, the above discussion may be used to anticipate the qualitative effect of propeller rotation rate. For higher rotation rates (lower magnitudes of J), the reverse flow induced by the propeller becomes stronger (relative to the free stream) and the vortex ring therefore moves upstream. The simulation results show the vortex ring core above the blade tips at $J = -0.5$ and moves progressively downstream at $J = -0.7$ and $J = -1.0$. In the limit of vanishingly small rotation rate ($J \to -\infty$), the reverse flow would become vanishingly small and the propeller would behave like a bluff body in uniform flow. Conversely, in the limit of vanishingly small free-stream velocity ($J \to 0-$), the propeller would entrain the quiescent fluid and produce a jet in the $-x$ direction. The propeller loads therefore scale with ρU^2 for $J < -0.7$ and scale with $\rho n^2 D^2$ for $J > -0.7$.

Acknowledgements

This work was supported by the Office of Naval Research under ONR grant N00014-05-1-0003 with Dr K.-H. Kim as programme manager. Computing resources were provided by the Arctic Region Supercomputing Center (ARSC) of the High Performance Computing Modernization Program (HPCMP) and the Minnesota Supercomputing Institute (MSI). We are grateful to Dr S. Jessup, Dr M. Donnelly, Dr C. Chesnakas, and their colleagues at NSWCCD for providing us with experimental data. We would also like to express our gratitude to Dr P. Chang for useful discussions and Dr A. Verma for very helpful suggestions on the manuscript.

REFERENCES

AMIET, R. K. 1988 Thickness noise of a propeller and its relation to blade sweep. *J. Fluid Mech.* **192**, 535–560.

ANTONIA, R. A. 1981 Conditional sampling in turbulence measurement. *Annu. Rev. Fluid Mech.* **13**, 131–156.

BEDDHU, M., TAYLOR, L. K. & WHITFIELD, D. L. 1996 Strong conservative form of the incompressible Navier–Stokes equations in a rotating frame with a solution procedure. *J. Comput. Phys.* **128**, 427–437.

BERCHICHE, N. 2008 Numerical predictions of crashback propeller flow and loadings. In *Proceedings of the 8th International Conference on Hydrodynamics*. China Ocean Press.

BERNERO, S. 2000 A turbulent jet in counterflow. PhD thesis, Technische Universität Berlin.

BRIDGES, D. H., DONNELLY, M. J. & PARK, T. J. 2005 Experimental investigation of the submarine crashback maneuver. In *43rd AIAA Aerospace Sciences Meeting and Exhibit, Reno, Nevada*. American Institute of Aeronautics & Astronautics.

BRIDGES, D. H., DONNELLY, M. J. & PARK, T. J. 2008 Experimental investigation of the submarine crashback maneuver. *J. Fluids Engng* **130**.

CHANG, P., EBERT, M., YOUNG, Y. L., LIU, Z., MAHESH, K., JANG, H. & SHEARER, M. 2008 Propeller forces and structural responses to crashback. In *Proceedings of the 27th Symposium on Naval Hydrodynamics, Seoul, Korea*. Curran Associates Inc.

CHAPMAN, C. J. 1988 Shocks and singularities in the pressure field of a supersonically rotating propeller. *J. Fluid Mech.* **192**, 1–16.

CHEN, B. & STERN, F. 1999 Computational fluid dynamics of four quadrant marine propeller flow. *J. Ship Res.* **43** (4), 218–228.

COOPER, A. J. & PEAKE, N. 2005 Upstream-radiated rotor–stator interaction noise in mean swirling flow. *J. Fluid Mech.* **523**, 219–250.

DAVOUDZADEH, F., TAYLOR, L. K., ZIERKE, W. C., DREYER, J. J., MCDONALD, H. & WHITFIELD, D. L. 1997 Coupled Navier–Stokes and equations of motion simulation of submarine maneuvers, including crashback. In *Proceedings of the 1997 ASME Fluids Engineering Division Summer Meeting, New York*. American Society of Mechanical Engineer.

DONNELLY, M., JESSUP, S. & ETEBARI, A. 2008 Measurement of steady and unsteady duct loads for propeller 4381 at crashback conditions in the 36 water tunnel. *Tech. Rep.* NSWCCD-50-TR-2008. Naval Surface Warfare Center.

DREES, J. M. & HENDAL, W. P. 1951 Airflow patterns in the neighbourhood of helicopter rotors: a description of some smoke tests carried out in a wind-tunnel at Amsterdam. *Aircraft Engineering and Aerospace Technology* **23** (4), 107–111.

DUTTWEILER, M. E. & BRENNEN, C. E. 2002 Surge instability on a cavitating propeller. *J. Fluid Mech.* **458**, 133–152.

EBERT, M., CHANG, P. & MULVIHILL, L. 2007 NSWCCD FY07 crashback computational effort. In *ONR Propulsor S & T Program Review*, October 2007.

FELLI, M., DI FELICE, F., GUJ, G. & CAMUSSI, R. 2006 Analysis of the propeller wake evolution by pressure and velocity phase measurements. *Exp. Fluids* **41**, 441–451.

FURUYA, O. 1985 A performance-prediction theory for partially submerged ventilated propellers. *J. Fluid Mech.* **151**, 311–335.

GERMANO, M., PIOMELLI, U., MOIN, P. & CABOT, W. H. 1991 A dynamic subgrid-scale eddy viscosity model. *Phys. Fluids* A **3** (7), 1760–1765.

GREEN, R. B., GILLIES, E. A. & BROWN, R. E. 2005 The flow field around a rotor in axial descent. *J. Fluid Mech.* **534**, 237–261.

HAMPTON, G. A. 1995 Open water force and moment characteristics on three propellers in a crashback condition. *Tech. Rep.* CRDKNSWC/HD-1126-NV. David Taylor Naval Ship Research and Development Center.

HECKER, R. & REMMERS, K. 1971 Four quadrant open-water performance of propellers 3710, 4024, 4086, 4381, 4382, 4383, 4384 and 4426. *Tech. Rep.* PNSRADC 417-H01. David Taylor Naval Ship Research and Development Center.

JESSUP, S., CHESNAKAS, C., FRY, D., DONNELLY, M., BLACK, S. & PARK, J. 2004 Propeller performance at extreme off design conditions. In *Proceedings of the 25th Symposium on Naval Hydrodynamics, St. John's, Canada*. National Academies Press.

JESSUP, S., FRY, D. & DONNELLY, M. 2006 Unsteady propeller performance in crashback conditions with and without duct. In *Proceedings of the 26th Symposium on Naval Hydrodynamics, Rome, Italy*. National Academies Press.

JIANG, C. W., DONG, R. R., LUI, H. L. & CHANG, M. S. 1997 24-inch water tunnel flow field measurements during propeller crashback. In *Proceedings of the 21st Symposium on Naval Hydrodynamics, Trondheim, Norway*. National Academies Press.

KINNAS, S. A. & FINE, N. E. 1993 A numerical nonlinear analysis of the flow around two- and three-dimensional partially cavitating hydrofoils. *J. Fluid Mech.* **254**, 151–181.

LEISHMAN, J. G. 2006 *Principles of Helicopter Aerodynamics*, 2nd edn. Cambridge University Press.

LILLY, D. K. 1992 A proposed modification of the Germano subgrid-scale closure model. *Phys. Fluids* A **4** (3), 633–635.

MAHESH, K., CONSTANTINESCU, G. & MOIN, P. 2004 A numerical method for large-eddy simulation in complex geometries. *J. Comput. Phys.* **197** (1), 215–240.

MAJETY, K. S. 2003 Solutions to the Navier–Stokes equations in non-inertial reference frame. Master's thesis, Mississippi State University.

NIAZI, S. 2000 Numerical simulation of rotating stall and surge alleviation in axial compressors. PhD thesis, Georgia Institute of Technology.

PAMPREEN, R. C. 1993 *Compressor Surge and Stall*. Concepts ETI, Inc.

PARRY, A. B. 1995 The effect of blade sweep on the reduction and enhancement of supersonic propeller noise. *J. Fluid Mech.* **293**, 181–206.

SHARIFF, K. & LEONARD, A. 1992 Vortex rings. *Annu. Rev. Fluid Mech.* **24**, 235–279.

STAUBLI, T., GYARMATHY, G. & INDERBITZEN, A. Visualization of rotating stall in a full size water model of a single-stage centrifugal compressor. *La Houille Blanche* **3/4**, 40–45.

TAM, C. K. W. & SALIKUDDIN, M. 1986 Weakly nonlinear acoustic and shock-wave theory of the noise of advanced high-speed turbopropellers. *J. Fluid Mech.* **164**, 127–154.

VERMA, A., JANG, H. & MAHESH, K. 2012 Large eddy simulation of flow around a reverse rotating propeller. *J. Fluid Mech.* **704**, 61–88.

VYŠOHLID, M. & MAHESH, K. 2006 Large eddy simulation of crashback in marine propellers. In *Proceedings of the 26th Symposium on Naval Hydrodynamics, Rome, Italy*. National Academies Press.

VYŠOHLID, M. & MAHESH, K. 2007 Understanding crashback in marine propellers using an unsteady actuator disk model. In *45th AIAA Aerospace Sciences Meeting and Exhibit, Reno, Nevada*. American Institute of Aeronautics & Astronautics.

YODA, M. & FIEDLER, H. E. 1996 The round jet in a uniform counterflow: flow visualization and mean concentration measurements. *Exp. Fluids* **21**, 427–436.